Materials Science & Engineering C xxx (xxxx) xxx

Contents lists available at ScienceDirect

Materials Science & Engineering C

journal homepage: www.elsevier.com/locate/msec

Delayed alveolar clearance of nanoparticles through control of coating composition and interaction with lung surfactant protein A

Susana Carregal-Romero [a,b,1], Hugo Groult [c,1], Olga Cañadas [d], Noelia A-Gonzalez [e,f], Ana Victoria Lechuga-Vieco [a,e,g], Belén García-Fojeda [d], Fernando Herranz [h], Juan Pellico [a,i], Andrés Hidalgo [e], Cristina Casals [d,*], Jesús Ruiz-Cabello [a,b,j,**]

[a] Centro de Investigación Biomédica en Red de Enfermedades Respiratorias (CIBERES), Instituto de Salud Carlos III, Madrid 28029, Spain
[b] Center for Cooperative Research in Biomaterials (CIC biomaGUNE), Basque Research and Technology Alliance (BRTA), Donostia-San Sebastián 20014, Spain
[c] BCBS team (Biotechnologies et Chimie des Bioressources pour la Santé), LIENSs Laboratory (Littoral Environment et Sociétés), UMR CNRS 7266, University of La Rochelle, La Rochelle 17000, France
[d] Universidad Complutense de Madrid, Departamento de Bioquímica y Biología Molecular, Madrid 28040, Spain
[e] Centro Nacional de Investigaciones Cardiovasculares Carlos III, Department of Cardiovascular Development and Repair (DRC), Madrid 28029, Spain
[f] Westfälische Wilhems University of Münster, Institute of Immunology, Münster 48149, Germany
[g] The Kennedy Institute of Rheumatology, NDORMS, University of Oxford, Oxford OX3 7FY, UK
[h] NanoMedMol, Instituto de Química Médica, Consejo Superior de Investigaciones Científicas (IQM-CSIC), Madrid 28006, Spain
[i] King's College London, School of Biomedical Engineering and Imaging Sciences, London SE1 7EH, UK
[j] Universidad Complutense de Madrid, Departamento de Química en Ciencias Farmacéuticas, Madrid 28040, Spain

ARTICLE INFO

Keywords:
Micellar superparamagnetic iron oxide nanoparticles
Pulmonary administration
Magnetic resonance imaging
Lung clearance
Surfactant protein A

ABSTRACT

The coating composition of nanomedicines is one of the main features in determining the medicines' fate, clearance, and immunoresponse in the body. To highlight the coatings' impact in pulmonary administration, two micellar superparamagnetic iron oxide nanoparticles (SPION) were compared. These nanoparticles are similar in size and charge but have different coatings: either phosphatidylcholine (PC-SPION) or bovine serum albumin (BSA-SPION). The aim of the study was to increase the understanding of the nano-bio interaction with the cellular and non-cellular components of the lung and underline valuable coatings either for local lung-targeted drug delivery in theranostic application or patient-friendly route systemic administration. PC-SPION and BSA-SPION were deposited in the alveoli by *in vivo* instillation and, despite the complexity of imaging the lung, SPION were macroscopically visualized by MRI. Impressively, PC-SPION were retained within the lungs for at least a week, while BSA-SPION were cleared more rapidly. The different lung residence times were confirmed by histological analysis and supported by a flow cytometry analysis of the SPION interactions with different myeloid cell populations. To further comprehend the way in which these nanoformulations interact with lung components at the molecular level, we used fluorescence spectroscopy, turbidity measurements, and dynamic light scattering to evaluate the interactions of the two SPION with surfactant protein A (SP-A), a key protein in setting up the nanoparticle behavior in the alveolar fluid. We found that SP-A induced aggregation of PC-SPION, but not BSA-SPION, which likely caused PC-SPION retention in the lung without inducing inflammation. In conclusion, the two SPION show different outcomes from interaction with SP-A leading to distinctive fate in the lung. PC-SPION hold great promise as imaging and theranostic agents when prolonged pulmonary drug delivery is required.

* Correspondence to: C. Casals, Departamento de Bioquímica y Biología Molecular, Universidad Complutense de Madrid, Jose Antonio Novais 12, 28040 Madrid, Spain.
** Correspondence to: J. Ruiz-Cabello, CIC biomaGUNE, Molecular and Functional Biomakers Laboratory, Parque Científico y Tecnológico de Gipuzkoa, Paseo Miramón 182, 20014 Donostia/San Sebastián, Gipuzkoa, Spain.
E-mail addresses: scarregal.ciberes@cicbiomagune.es (S. Carregal-Romero), hugo.groult@univ-lr.fr (H. Groult), ocanadas@ucm.es (O. Cañadas), alonsogo@uni-muenster.de (N. A-Gonzalez), ana.lechuga-vieco@kennedy.ox.ac.uk (A.V. Lechuga-Vieco), bgarciafojeda@pdi.ucm.es (B. García-Fojeda), fherranz@iqm.csic.es (F. Herranz), juan.pellico@kcl.ac.uk (J. Pellico), ahidalgo@cnic.es (A. Hidalgo), ccasalsc@ucm.es (C. Casals), jruizcabello@cicbiomagune.es (J. Ruiz-Cabello).
[1] These authors contributed equally to the work.

https://doi.org/10.1016/j.msec.2021.112551
Received 11 August 2021; Received in revised form 3 November 2021; Accepted 10 November 2021
Available online 14 November 2021

1. Introduction

The lung is one of the organs prone to non-parenteral direct entry routes. Inhalation, and to a lesser extent intranasal or intra-tracheal administration [1,2], have thus become the desired routes for treating in the first place pulmonary diseases. Indeed, pulmonary drug delivery allows for direct local targeting of the lungs gather with many advantages over the other administration routes [3,4]. Thus, drugs can be delivered into the lungs with uniform distribution and several additional advantages: i) avoid a first-pass metabolism; ii) take a rapid onset of action; and iii) reach high local concentrations with lower doses and less toxicity. Pulmonary drug delivery can also be considered as a promising alternative for systemic delivery due to the relatively easy and rapid absorption of the molecules through the extended thin alveolar epithelial layer and subsequent translocation into the bloodstream. For all of these reasons, this administration route has gained increasing interest and has been the subject of numerous pre-clinical studies [5,6].

Nanoparticle (NP)-based therapies offer many advantages over non-nano drug formulations, particularly the possibility of protecting labile drugs such as RNA vaccines or integrating multiple functions such as imaging modality for theranostic applications. They have enhanced therapeutic options such as codelivery of multiple drugs, reduced side effects, controlled drug release, and enhanced cellular targeting [7,8]. However, because of their nanometric size and high surface to volume reactivity, NP fate, and lung immune response can be completely different compared to lung delivery of simple drug molecules. Thus, their application is regarded with caution. In the past few decades, studies of the interaction of inhaled NP with the lungs have been focused primarily on determining the toxicity of specific compositions for eco-environmental toxicological studies [9] or their potential application in clinical drug delivery [5]. Convectional and diffusional mechanisms can efficiently help depositing inhaled or instilled NP in all lung regions with the proper size and delivery technology [4]. Using the correct methodology and NP surface engineering, they can provide sustained release in lung tissue. Due to the high bioavailability across the alveolar epithelium, this patient-friendly administration route is also an alternative to systemic or local therapy with reduced dosage [1,5]. Many formulations of different kinds of NP (biodegradable natural or synthetic polymeric, protein-, lipid- and metallic-based) have been reported for pulmonary administration [5,6,10,11]. Some of them have been investigated for several pulmonary diseases, including cystic fibrosis, asthma, chronic obstructive pulmonary disease, lung infections, lung cancer, and others under consideration or are currently being developed to treat many other non-lung related diseases [10,12,13]. These studies have looked mainly at the influence of type, size, charge, shape, or other features in the overall clearance of the NP [14]. Nevertheless, few examples have given details of NP's molecular interaction with alveolar components and its impact on the biodistribution and clearance from the lungs [15]. Especially with SP-A, a versatile lipid-binding recognition protein present in the alveolar fluid, a component of the lung surfactant corona and involved in lung defense, which has an essential role in NP opsonization [16–19]. Also, very few *in vivo* imaging applications have been described, probably due to the intrinsic difficulty of imaging this organ in continuous motion and mainly composed of air [6,20–25].

Our work demonstrates the possibility of applying micellar superparamagnetic iron oxide nanoparticles (SPION), coated with two clinically suitable excipients as model nanomedicines, to visualize them *in vivo* by magnetic resonance imaging (MRI) and compare the coating effect on their fate, clearance, and interaction with alveolar components after pulmonary administration. The SPION formulations had similar sizes and charges but different coatings: bovine serum albumin (BSA) and phosphatidylcholine (PC). Because it is possible to load our micelles with hydrophobic drugs or dyes, we used fluorescence labeling as a strategy to confirm the MRI results with flow cytometry. We performed an analysis at different time points of the SPION interactions with the alveolar macrophages and the composition of the myeloid cells' population on the whole lung tissue. Finally, to appreciate the differences observed between the differently coated micellar SPION we did a complete study of their interaction with SP-A and the impact on its immunomodulatory action.

2. Materials and methods

2.1. Synthesis and characterization of PC-SPION and BSA-SPION

The synthesis of micellar PC-SPION and BSA-SPION and their complete characterization methods have been described earlier. In brief, oleic acid-coated SPION were prepared following the protocol described by Yu et al. [26] and subsequently transferred to water through their coating with two different kinds of amphiphilic molecules: Bovine Serum Albumin (purchased from Merck Group, Darmstadt, Germany, CAS N° 9048-46-8, ref: A2153) and L-α-phosphatidylcholine from egg yolk (from Sigma-Aldrich (St Louis, Missouri, USA), CAS N° 8002-43-5, ref: 61755) [27,28]. Egg PC is a mixture of different phosphatidylcholine molecular species. Analysis of the profile composition of fatty acids in PC from egg yolk shows that the fatty acids are mainly saturated (44.8%) and monounsaturated (40.6%), with a small fraction (14.6%) of polyunsaturated fatty acids [29]. The hydrodynamic size, polydispersity index, and zeta potential of the SPION were measured with a Zetasizer Nano ZS90 (Malvern Instruments, UK). Morphology and core size were determined using transmission electron microscopy (TEM) at a JEM 1400PLUS (JEOL), equipped with a LaB6 filament, and operated at 120 kV acceleration voltage. Diluted magnetic SPION suspensions were placed on carbon film-coated copper grids. Their solvent was evaporated at room temperature for 24 h. Negative staining was achieved by dropping 10 μL of an aqueous solution of uranyl acetate (UA) on TEM grids containing dried diluted solutions of the two different micellar SPION followed by incubation for 1 min and drying of the UA drop with a filter paper, similarly to the protocol described by Robin Harris [30]. Fourier transform infrared spectroscopy (FT-IR) spectra were obtained on a Perkin Elmer Spectrum 400 Series spectrometer (Perkin Elmer, USA). Thermogravimetric analysis (TGA) spectra were obtained with a Seiko TG/ATD 320 U, SSC 5200 (Seiko Instruments, Japan). The dried PC-SPION or BSA-SPION were heated from 20 °C to 1000 °C at 10 °C/min under an airflow of 100 mL/min. Mass spectrometry was performed in a Bruker Esquire 3000 apparatus (Bruker Daltonik, Germany) equipped with an ESI source and an ion trap analyzer, coupled to an Agilent 1100 capillary LC system (Agilent Technologies, USA). The sample was diluted 1/10 in water/methanol (1:1) before the LC/MS analysis. The analyses were carried out by FIA (flow injection analysis), working in both polarities, using a 0.1% formic acid/methanol (50/50) mix as the mobile phase to promote ionization, at 0.1 mL/min.

For some experiments, PC-SPION were fluorescently labeled with the lipophilic probe carbocyanine DiI-C18 (λ_{ex}: 549 nm; λ_{em}: 565 nm) and BSA was conjugated with Alexa Fluor 647 fluorophore (λ_{ex}: 650 nm; λ_{em}: 670 nm). These modifications did not alter the surface properties of the micelles, especially their hydrodynamic sizes and zeta potential, as we have already shown in previous works [27,31].

2.2. Preparation of phosphatidylcholine vesicles

Unilamellar vesicles of dipalmitoylphosphatidylcholine (DPPC) (Avanti Polar Lipids, Birmingham, AL, USA) were prepared as previously described [32–34]. Briefly, the required amounts of DPPC dissolved in chloroform/methanol (3:1 *v*/v) were evaporated to dryness under a gentle stream of nitrogen, and solvent traces were removed by evacuation under reduced pressure overnight. DPPC vesicles were prepared at a phospholipid concentration of 1 mg/mL by hydrating dry lipid films in a buffer containing 5 mM Tris-HCl pH 7.4 and 150 mM NaCl and swelling for 1 h at 50 °C, above the gel-to-liquid phase transition of DPPC. After vortexing, the resulting multilamellar vesicles were sonicated at the same temperature for 10 min at 390 W/cm^2 (burst of

0.6 s, with 0.4 s between bursts) in a UP 200S sonicator with a 2 mm microtip. The final lipid concentration was assessed by phosphorus determination.

2.3. In vivo MRI imaging of PC-SPION and BSA-SPION lung biodistribution after i.t. administration

Male C57BL/6 mice provided from Janvier Labs ($n = 3$), eight weeks-old weighting 25 g, were used for MRI experiments. Mice were anesthetized using 2% isoflurane and maintained anesthetized *via* facial mask all the experiment. For instillation, intratracheal intubation was performed on the mice using a 22-Gauge Teflon intravenous catheter. The catheter was passed through the vocal cords into the trachea's beginning and positioned just before the carina. 50 μL of SPION contrast agent ([Fe] = 0.6 mg/mL) were deposited through the tracheal catheter. The contrast agent's solution was obtained by dissolving the SPION in saline solution (0.9% NaCl) to reach the desired concentration. After extubation, an MRI of the mice's lungs was acquired at different times, from 1 h up to 6 days. The images were acquired with a 7 T spectrometer (Bruker, Ettlingen, Germany), using a transmitter/receiver quadrature coil of 25 mm inner diameter (Bruker, Ettlingen, Germany). Mice were placed prone in a custom-built plastic holder and kept anesthetized with the same (2%) isoflurane conditions in a mixture of N_2/O_2 (80:20) *via* a facial mask. The body temperature was kept constant at 37 °C using a warm air blower feedback and a rectal probe, with constant respiration monitoring with an MRI compatible equipment (SAII, SA Instruments). One ultra-short echo time (UTE) axial slice positioned immediately above the diaphragm of 1 mm thickness was acquired for each animal, and ten consecutive coronal gradient-echo slices of 1 mm thickness to cover lung, liver, spleen, and kidney. Both acquisitions were performed with ten averages and respiratory gating. For UTE imaging, two consecutive 1 mm thick axial slices were acquired 2D multislice sequence (804 directions/256 points) with echo time (TE) of 468 μs, repetition time (TR) of 30 ms, a bandwidth of 100 kHz, flip angle (FA) of 15 degrees and field of view (FOV) of 3.5 cm × 3.5 cm. The total acquisition time for ten averages was of about 4 min. For gradient-echo acquisitions, we also averaged ten times using respiratory gating and ten consecutive coronal slices using gradient-echo FLASH sequence with 4/100 ms TE/TR, 30 degrees FA, and a 4.5 × 2.8 cm FOV with 256 × 128 points.

2.4. Ethics committee approval

All the experimental procedures were approved by the Animal Care and Ethics Committee of CIC biomaGUNE and the regional authorities.

2.5. Ex-vivo analysis of PC-SPION and BSA-SPION after i.t. administration in the lung

For these experiments, six to twelve weeks old C57BL/6 male and CD1 female mice were used throughout the study. Mice were lightly anesthetized with 2.0% isoflurane (Abbott, Cham, Switzerland) delivered in a box. 0.25 mg/kg of each SPION in 25 μL of saline (0.9%) or vehicle (25 μL of saline (0.9%)) was intratracheally administered with a micropipette.

2.5.1. Histological analysis

Histological analysis of SPION biodistribution in lung, liver, and kidney tissues was performed two days post-administration. Briefly, organs were extracted and fixed in 4% paraformaldehyde before being embedded in paraffin blocks. Sections were deparaffinized and rehydrated before staining with Perls' Prussian blue to detect iron oxide cores.

2.5.2. Flow cytometry analysis

Mice ($n = 3$ for each group) were euthanized by intraperitoneal pentobarbital administration (60 mg/mL), and lungs were harvested and placed in HBSS. Whole lung tissue was digested in HBSS with liberase (1 U/mL, Roche) and DNAse I (10-3 U/mL, Sigma) for 30 min at 37 °C. Single-cell suspensions were then incubated with the indicated antibodies for 15–20 min at 4 °C. Phenotyping antibodies against CD45, CD11b, F4/80, SiglecF, Ly6G, CD103, CD11c, and MHCII were used for myeloid cells. Samples were acquired in an LSRII Fortessa (BDBiosciences). Doublets and DAPI+ cells were excluded from analyses using the FlowJo software (Flowjo LLC, Ashland, OR).

2.6. SPION uptake by macrophage

RAW264.7 macrophages (40×10^4 cells/well) were seeded for 24 h. Next, they were incubated with SPION micelles at the concentration [Fe] = 0.06 mg/mL in complete DMEM medium for a further 24 h. Cells were washed with PBS, fixed with 4% (*w/v*) paraformaldehyde for 20 min and stained with 2% potassium ferrocyanide II/1 M hydrochloric acid mixture (1:1) for 10 min at 37 °C. Finally, after additional washes with PBS, they were counterstained with nuclear fast red solution (0.1%, w/v) for 10 min.

2.7. Isolation, purification, and characterization of human SP-A

Surfactant protein A was isolated from bronchoalveolar lavage of patients with alveolar proteinosis using the sequential butanol and octylglucoside extraction [32–34]. Endotoxin content of isolated human SP-A was about 300 pg endotoxin/mg SP-A as determined by Limulus amebocyte lysate assay (Lonza, Basel, Switzerland). The purity of SP-A was checked by one-dimensional SDS-PAGE in 12% acrylamide under reducing conditions and mass spectrometry. SP-A consisted of supratrimeric oligomers of at least 18 subunits (Mw, 650 kDa). The oligomerization state of SP-A was assessed by electrophoresis under nondenaturing conditions, electron microscopy, and analytical ultracentrifugation as reported elsewhere [32–34].

2.8. Fluorescence assays to determine the binding of SP-A to SPION

The stock solutions of micellar PC-SPION and BSA-SPION were sonicated for 10 min using an Ultrason 6 bath sonicator (JP Selecta, Spain) before their use. SPION molar concentration was calculated as the number of SPION per liter/Avogadro number. Fluorescence measurements were conducted in an SLM-Aminco AB-2 spectrofluorimeter with a thermostated cuvette holder (Thermo Spectronic, Waltham, MA, USA), using 5 × 5 mm path-length quartz cuvettes. All measurements were performed at 25.0 ± 0.1 °C. Fluorescence intensity experiments were designed to characterize the binding of SP-A to both SPION and DPPC vesicles, as previously reported [32]. For PC-SPION and DPPC vesicles, samples of 17.5 nM SP-A were titrated with different amounts of a stock solution of PC-SPION or DDPC vesicles. Samples were allowed to interact for 10 min, and the emission spectrum of SP-A was recorded with excitation at 295 nm. The background intensity due to light scattering by SP-A, PC-SPION, or DPPC vesicles was subtracted from each recording of the fluorescence intensity of SP-A. For analysis of SP-A binding to BSA-SPION, Alexa 647-labeled BSA-SPION (93 nM) were titrated with increasing amounts of SP-A, and the emission spectra of the fluorescent dye were recorded 10 min after the addition of SP-A upon excitation at 594 nm. The background intensity was subtracted from each recording of the fluorescence intensity of Alexa 647. The effect of dilution on the fluorescence of either Alexa 647-labeled BSA-SPION or SP-A tryptophan was corrected by the addition of buffer to either Alexa 647-labeled BSA-SPION or SP-A samples, respectively. The apparent dissociation constant (K_D) at 25 °C for the complexes of PC-SPION and DPPC vesicles with SP-A was obtained by analyzing the change in SP-A fluorescence at 335 nm upon addition of increasing amounts of NP. The binding titration data were analyzed by nonlinear least-squares fitting to the Hill equation as described [35]:

$$\Delta F = \Delta F_{max} \cdot \frac{[L]^{nH}}{K_D + [L]^{nH}}$$

where ΔF is the change in fluorescence intensity at 335 nm relative to the intensity of free PC-SPION; $\Delta Fmax$ is the change in fluorescence intensity at saturating SPION or DPPC concentrations; K_D is the apparent equilibrium dissociation constant; $[L]$ *is* the molar concentration of free SPION or DPPC vesicles; and n_H is the Hill coefficient. A similar analysis was performed to assess K_D for complexes of BSA-SPION with SP-A by analyzing the change in the fluorescence at 672 nm of Alexa 647-labeled BSA-SPION upon addition of increasing amounts of SP-A.

2.9. Aggregation assays

2.9.1. Turbidity measurements

SP-A and calcium's effects on the aggregation of PC-SPION was determined by measuring the change in absorbance at 400 nm in a Beckman DU-800 spectrophotometer [36]. Briefly, PC-SPION or DPPC vesicles were added to both the sample and the reference cuvettes in 5 mM Tris-HCl and 150 mM NaCl buffer, pH 7.4. After 10 min equilibration at 37 °C, human SP-A was added to the sample cuvette, and the change in optical density at 400 nm was monitored. Next, Ca^{2+} was added to both the sample and reference cuvettes, and the change in absorbance was monitored again. Final concentrations of SPION, phospholipids, SP-A, and calcium were 30 μg/mL, 30 μg/mL, 40 μg/mL (61 nM), and 2.5 mM, respectively.

2.9.2. Dynamic Light Scattering (DLS)

The effect of SP-A on the agglomeration behavior of BSA- and PC-SPION and DPPC vesicles was depicted in terms of size distribution at 25 °C using DLS [35,37,38]. Briefly, 50 μg/mL of SPION (either PC-SPION or BSA-SPION) or 80 μg/mL of DPPC were mixed with increasing amounts of SP-A in phosphate buffer, pH 7.4, containing 150 mM NaCl (PBS). Samples were allowed to interact for 10 min and then were measured in a Zetasizer Nano S (Malvern Instruments, Malvern, UK) equipped with a 633-nm HeNe laser as previously described [35,37]. BSA (40 μg/mL) (0.6 μM) was measured to control the size distribution of the free protein. Four scans were recorded for each sample, and all the samples were analyzed in triplicate. The general purpose and the multiple narrow modes algorithms available from the Malvern software for dynamic light scattering analysis were used to determine the effect of SP-A on the intensity-based size distribution and the hydrodynamic diameter (*Z*-average) of the nanomaterials. Experiments were performed in the presence and absence of calcium. Alternatively, samples used for turbidity measurements were also analyzed by DLS.

2.10. Determination of TNF-α release by ex-vivo cultured rat alveolar macrophages

Bronchoalveolar lavage from Sprague Dawley male rat lungs was obtained as previously reported with some modifications [38,39]. Rats (approximately 350 g) were killed in a CO_2 chamber, and the cardiopulmonary block was extracted to perform bronchoalveolar lavages with PBS, 0.2 mM EDTA. All animals received humane care following the Guide for the Care and Use of Laboratory Animals and Spanish guidelines for experimental animals. Cells were separated by centrifugation (250 ×*g*, 10 min) and were washed twice with PBS. The cell pellet was resuspended in RPMI 1640 medium (10% heat-inactivated FBS, 100 U/mL penicillin, 100 μg/mL streptomycin, supplemented with glutamine 2 mM) (Lonza). Rat aMϕs were purified by adherence for 90 min at 37 °C under a 95% air-5% CO_2 atmosphere in 150-cm^2 culture flasks as previously reported [38,39]. Adherent aMϕs were gently scraped, plated in 96-well plastic dishes (7.5×10^4 cells per well) in 0.2 mL of RPMI with 5% FBS, and precultured overnight. Before the stimulation of the cells, SP-A was incubated for 10 min at room temperature in the presence of BSA-SPION or PC-SPION at a weight ratio of 1:1 (SP-A:BSA-SPION) and 11.4:1 (SP-A:PC-SPION). Then, cells were incubated for 24 h in the presence or absence of smooth LPS (*Escherichia coli* 055:B5, 1 ng/mL) (Sigma, St. Louis, Missouri), rat recombinant IFN-γ (Calbiochem, Darmstadt, Germany) (10 ng/mL), SP-A (77 nM), BSA- or PC-SPION (56 nM and 11 μM, respectively), and combinations thereof. Cell viability was higher than 95% under assay conditions. Macrophage cultures were plated in triplicate wells, and each series of experiments was repeated at least three times. Measurement of TNF-α production in supernatants of rat aMϕs was performed using specific ELISA kit following the supplier's instructions (BD Biosciences, San Diego, CA) [34,38–40]. *Statistics*: Data are presented as means ± SEM. Differences in means between groups were evaluated by one-way ANOVA followed by the Bonferroni multiple-comparison test. An α level ≤ 5% ($P \leq 0.05$) was considered significant.

2.11. Bacterial killing assay

Escherichia coli J5 bacteria (American Type Culture Collection, Manassas, Virginia) were grown in Luria-Bertani broth at 37 °C with continuous shaking to exponential phase. Bacteria were then harvested, resuspended in PBS, and adjusted to the desired final concentration. The microbicidal activity of SP-A alone and bound to PC- or BSA-SPION was evaluated by colony counting on plate assays as previously described [35]. Before the incubation with bacteria, SP-A was incubated for 10 min at room temperature in the presence of BSA-SPION or PC-SPION at a weight ratio of 1:1 (SP-A:BSA-SPION) and 11.4:1 (SP-A:PC-SPION). Five microliters of bacterial suspension (10^5 CFU/mL) were incubated with different concentrations of SP-A, SPION, or combinations thereof in 30 μL of Hank's balanced salt solution buffer (137 mM NaCl, 5.4 mM KCl, 0.25 mM Na_2HPO_4, 0.44 mM KH_2PO_4, 1.3 mM $CaCl_2$, 1 mM $MgSO_4$, 4.2 mM $NaHCO_3$). Incubations were performed at 37 °C, for 30 min, with intermittent gentle shaking of 30 s every 5 min. At the end of incubation, bacterial suspensions were plated on LB agar plates and incubated for 18 h at 37 °C. Viable bacteria were enumerated by colony count.

3. Results

3.1. In vitro characterization of micellar PC-SPION and BSA-SPION

PC- and BSA-SPION were synthesized from oleic acid-coated SPION according to previously published methods [27,28]. Briefly, hydrophobic SPION coated with oleic acid and dissolved in hexane were added to either PC or BSA dissolved in a large volume of phosphate buffer. After sonication, the organic phase was evaporated, and micellar SPION were formed (Fig. 1).

Fig. 2 and Table 1 show the result of the micellar SPION synthesis. The oleic acid-coated SPION before the encapsulation into micelles presented an average diameter (d_{TEM}) of 13 ± 2 nm measured with transmission electron microscopy (TEM) analysis (Fig. 2A-B). After the micellar structure formation, the hydrodynamic diameter (d_h) of BSA- and PC-SPION were approximately 125 nm (Fig. 2B and Table 1), measured with dynamic light scattering (DLS), which indicates the formation of NP groupings. With TEM, the micellar structure formation of both BSA- and PC-SPION (Fig. 2C-E respectively) was subtly observed unless negative staining is used. Aqueous uranyl acetate was used to resolve the solvent-excluded surface of such hybrid materials. These microphotographs revealed the micellar structure with a large organic coating and a heterogeneous number of encapsulated SPION in both kinds of micelles (Fig. 2D and F, respectively).

Both micelles displayed high stability in PBS and good blood biocompatibility, as already shown in previously published applications relying on intravenous administration [27,28]. We have also previously reported the cytotoxicity and internalization of BSA-SPION and PC-SPION on C57BL/6 mouse embryonic fibroblasts (MEFs) [27,28,31].

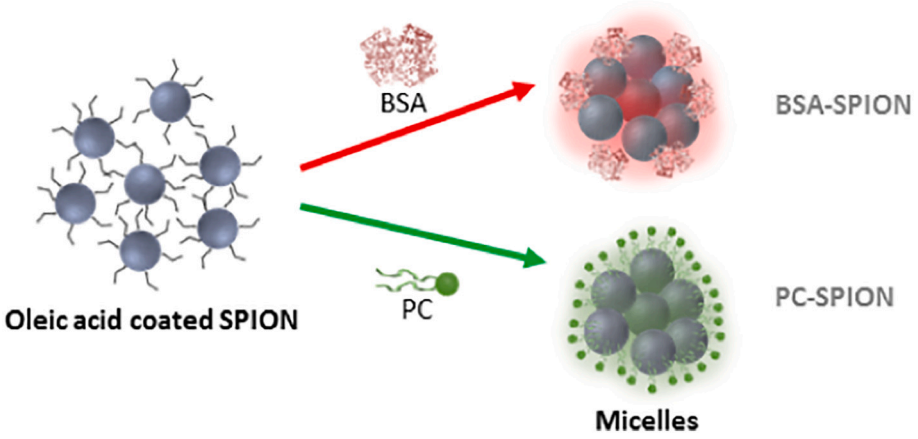

Fig. 1. Formation of water-soluble micellar SPION. Micellar structures were formed from hydrophobic oleic acid-coated SPION wrapped by two kinds of amphiphilic molecules: BSA and PC. For some experiments, PC-SPION were fluorescently labeled with the lipophilic probe carbocyanine DiI-C18 (λ_{ex}: 549 nm; λ_{em}: 565 nm) and BSA was conjugated with Alexa Fluor 647 fluorophore (λ_{ex}: 650 nm; λ_{em}: 670 nm), showing similar characteristics and hydrodynamic sizes to non-labeled NP.

For PC-SPION, the cell growth and viability analysis have shown cytotoxicity for the highest dose at 80 μg/mL and progressive uptake by MEFs along time (Fig. S1), suggesting that low-doses of nanoemulsion can be used safely *in vivo* as MRI contrast agents or drug carriers. For BSA-SPION, the cell growth and viability analysis have shown negligible cytotoxicity, and the uptake experiment revealed an effective internalization of the SPION (Fig. S2). This overall low toxicity was anticipated in front of the bio-acceptability of components BSA and phosphatidylcholine, already safely used in biomedical applications [41].

3.2. In vivo MRI

By *in vivo* MRI, we visualized these two magnetic NP types to determine if the different coatings affect trafficking across the alveolar-capillary barrier and residence times in the lung. Typically, proton-based MRI of the lung is complicated because of the constant cardiorespiratory motion, the magnetic susceptibility changes with multiple air-tissue interfaces, and the low proton density of its parenchyma. Thus, visualizing contrast agents, mostly negative or T2 contrast agents, in this organ is challenging, especially in high field magnets. Ultrashort echo (UTE) sequences allowed us to visualize the signal reduction changes in the mouse lung parenchyma after NP's intratracheal administration. Low signal intensities in this imaging modality correspond to airways and, when sufficiently accumulated, to locally deposited SPION due to the iron oxide cores' magnetic susceptibility effect. Nanoparticles were displayed only when they were aggregated (Fig. 3).

In parallel, complementary pseudo-colored gradient-echo coronal images highlighting the differences allowed us to visualize how these NP are translocated into the bloodstream and possibly distributed into other tissues (Fig. 4). The substantial negative signal enhancement observed in the liver, 2 or 6 days after BSA-SPION administration (arrows) indicated that the hepatic route is one of the essential clearance routes for these SPION even after direct lung administration. In the case of PC-SPION, in correspondence with the higher retention in the lung, the signal reduction was only observed in the liver on day 6 (white circle in Fig. 4). All these mechanisms are essential to design new nanomaterials and nanocarriers for lung administration [42]. Our results illustrate the importance of imaging to calculate the proportion of these nanomaterials that can be systemically found after inhalation or intrapulmonary administration. Quantitative data analysis of NP biodistribution was carried out by analyzing the normalized signal intensity against muscle in selected peripheral pulmonary regions (excluding central regions and large vessels) and additional regions of interests (ROIs) in the liver (Fig. S3). This imaging analysis is affected by the inter-day localization of these pulmonary areas and similar signal intensity in small and large airways. Yet, a clear decrease of signal intensity was obtained denoting the presence of the SPION in both organs. A visual inspection and localization of these signal voids in the lungs along the days facilitated the interpretation of these results, with higher accumulation in the PC-SPION nanoparticles (arrows in Fig. 3).

3.3. Ex-vivo analysis of PC- and BSA-SPION and their interaction with lung immune cells

Histopathology results of the lung at two days after instillation are summarized in Fig. S4. Images reveal a clear tendency of PC-SPION to cluster or aggregate within the alveolar lumen and alveolar duct, highlighted in blue by the Prussian Blue reagent reaction with iron. Co-localization with lung macrophages (stained with F4/80 antibody) was also detected. Contrary, a negligible amount of BSA-SPION was detected in the lungs. The different residence times of the BSA- and PC-SPION in the lung is supported by the analysis of SPION association with different lung myeloid cells at different times after intratracheal administration. For these experiments, we included a minor fraction of fluorescence labels (DiIC18 or AF647-BSA) in the coating to synthesize DiIC18-PC-SPION and AF647-BSA-SPION, respectively. These modifications did not alter the surface properties of the micelles, especially hydrodynamic size and zeta potential, as we have already shown previously [27,31]. An example of the flow cytometry cell sorting gating strategy is depicted in Fig. S5. Fig. 5 shows the percentage of aMϕs, interstitial macrophages, and dendritic cells associated with DiI-PC- and AF647-BSA-SPION at days 0, 2, and 6 after instillation. A fraction of aMϕs interacted with AF647-BSA-SPION just after instillation but rapidly disappeared, and no more fluorescent signal was detected on day 2. In contrast, DiI-PC-SPION remained associated with aMϕs 6 days after instillation. Significantly few resident interstitial macrophages were associated with any of these SPION. Control experiments to compare the uptake of BSA-SPION and PC-SPION by macrophages, were performed with murine macrophages (RAW 264.7). After 24 h of incubation with BSA- or PC-coated SPION nanoparticles, macrophages were fixed and stained with Perls Prussian blue (to detect the iron oxide cores) and counterstained with nuclear fast red solution (Fig. S6). With respect to BSA-SPION, images clearly showed that they were rapidly internalized. On the contrary, PC-SPION nanoparticles were only partially internalized and seemed to be more localized at the cell membrane.

Fig. 5 also shows that the acquisition of DiI fluorescence by dendritic cells (major histocompatibility complex class MHCII^{high} CD11c^{high}, CD103^{neg}, CD11b^{high}, and F4/80^{neg}) was visible on day 0 and 2, clearing at day 6. This result might suggest the migration of this discrete cell population to the draining lymph nodes to present antigens. However,

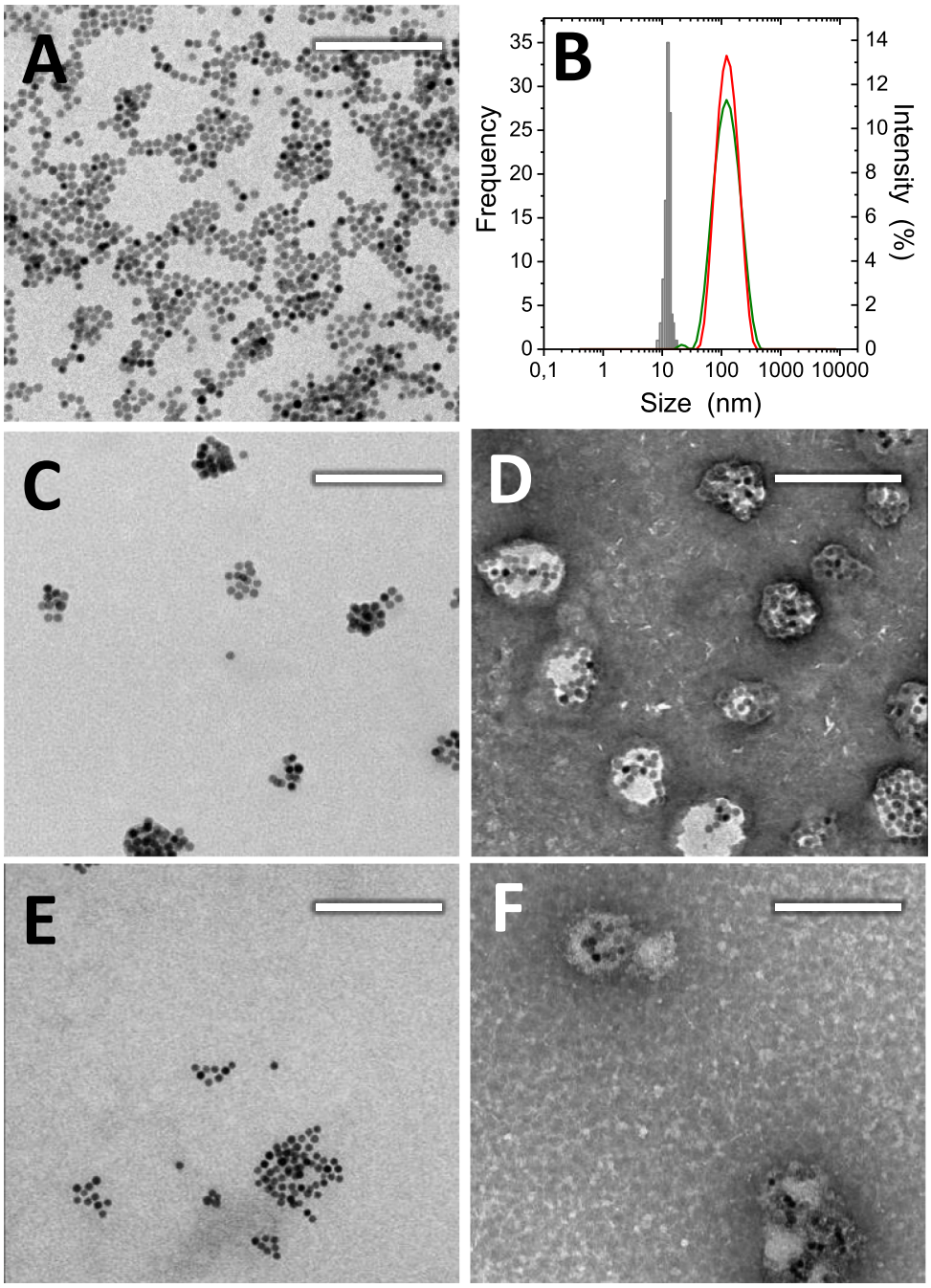

Fig. 2. Physicochemical characterization of the micellar SPION. (A) TEM image of monodisperse SPION coated with oleic acid. (B) Diameter (d_{TEM}) distribution of the SPION cores measured by TEM (left Y-axis) and hydrodynamic diameter (d_h) of BSA-SPION (red line) and PC-SPION (green line) measured by DLS (right axis). TEM images of (C) BSA-SPION, (D) negative stained BSA-SPION, (E) PC-SPION (F), and negative stained PC-SPION. All scale bars correspond to 200 nm. Table 1 collects the essential physicochemical characterization of BSA- and PC-SPION micelles. They were both similar in size and charge. Interestingly, these two different coatings caused substantial differences in the *in vivo* blood lifetime of the micellar SPION after i.v. administration (0.5 h for BSA-SPION *versus* more than 12 h for PC-SPION), as we have described in previous work [27,28,31]. (For interpretation of the references to colour in this figure legend, the reader is referred to the web version of this article.)

Table 1
BSA- and PC-SPION physicochemical characterization.

Nanoparticle	d_{TEM} (nm)	d_h (nm)	ζ-potential[a] (mV)
BSA-SPION	12.6 ± 1.4	125.4 ± 4	−19.7
PC-SPION	12.6 ± 1.4	125.3 ± 3	−11.5

[a] Measured at pH = 7.4.

lung draining lymph nodes were also analyzed at each time point, and neither DiI nor AF647 associated fluorescence was detected (not shown). Other populations analyzed in the lung were monocytes, neutrophils, and eosinophils, and none of them was found positive for any of the fluorochromes associated with the SPION at any time point.

The long retention time of PC-SPION in the lung raises the question of whether a prolonged lung exposition might trigger an inflammatory process. Therefore, we analyzed the percentage of inflammatory immune cell populations in lung lysates after treatment with PC- and BSA-SPION. We did not observe significant changes in the relative frequency of neutrophils, monocytes, and eosinophils after micellar SPION instillation (Fig. S7). We also checked the changes in MHCII and did not find any significant change in CD11b expression in aMϕs that could indicate macrophage activation. There was only a little shift in dendritic cells' population from migratory to the inflammatory state after one week. Further experiments indicated that the incubation of either PC- or BSA-SPION with isolated rat aMϕ in the absence of any stimulus, induced negligible TNF-α release, confirming their low propensity to provoke a proinflammatory response in aMϕ (see results of Fig. 9).

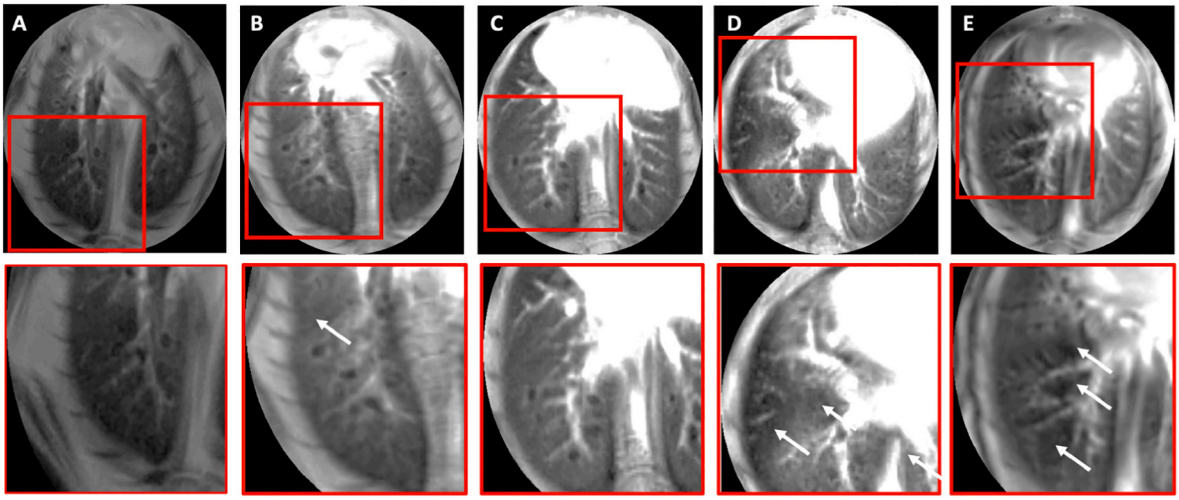

Fig. 3. *In vivo* MRI. Axial ultra-short echo time lung images of animal instilled with (A) saline; BSA-SPION at (B) 3 days and (C) 6 days post-instillation; and PC-SPION at (D) 3 days and (E) 6 days after administration. The lower panels display some enlarged areas with SPION. The arrows indicate the strongest decrease in contrast caused by these nanoparticles' presence, mainly PC-SPION (panels D and E).

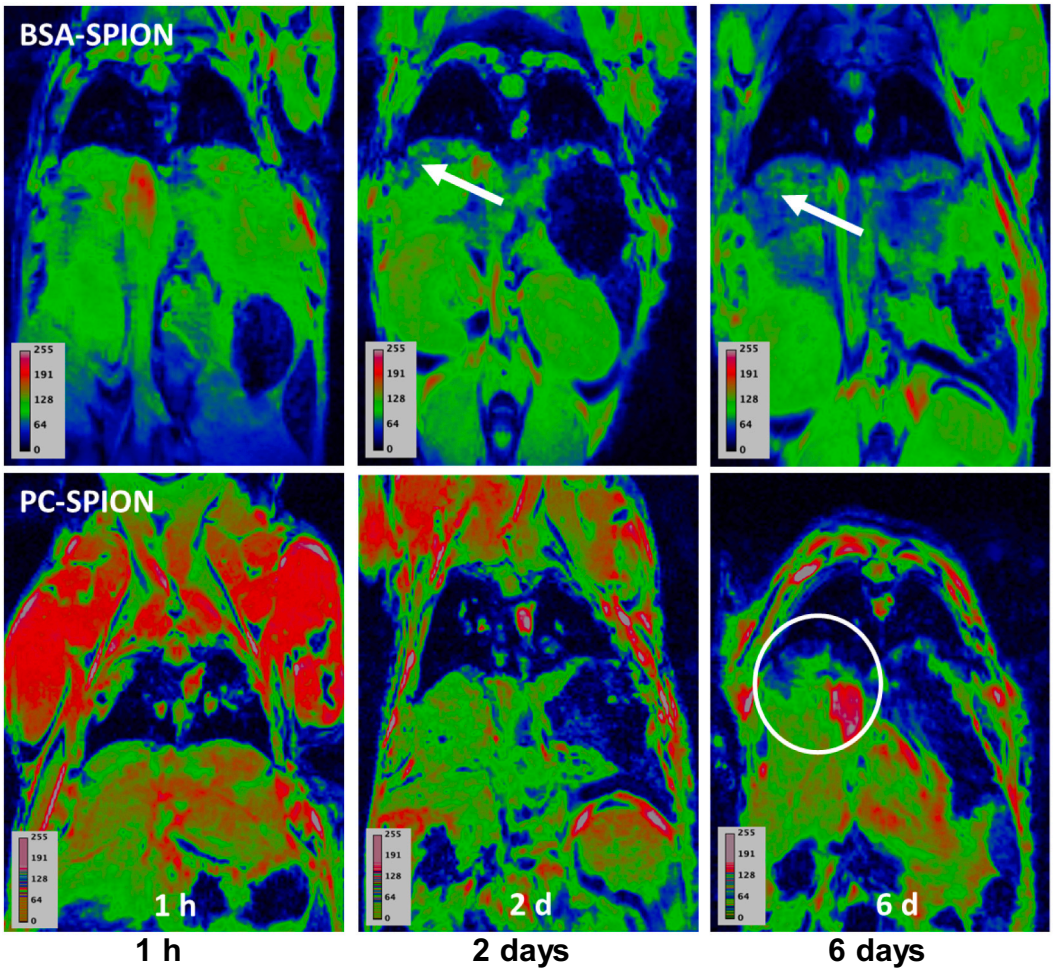

Fig. 4. Biodistribution of BSA-SPION and PC-SPION visualized *in vivo* by MRI. Parallel coronal gradient-echo images 1 h, 2 days and 6 days after the selective administration of contrast agent (50 μL; [Fe] = 0.6 mg/mL). The images are in pseudocolor scale to facilitate visualization of the negative contrast accumulation, showed by a blue signal in the liver (arrows) for BSA-SPION and the same areas (circle) for PC-SPION. (For interpretation of the references to colour in this figure legend, the reader is referred to the web version of this article.)

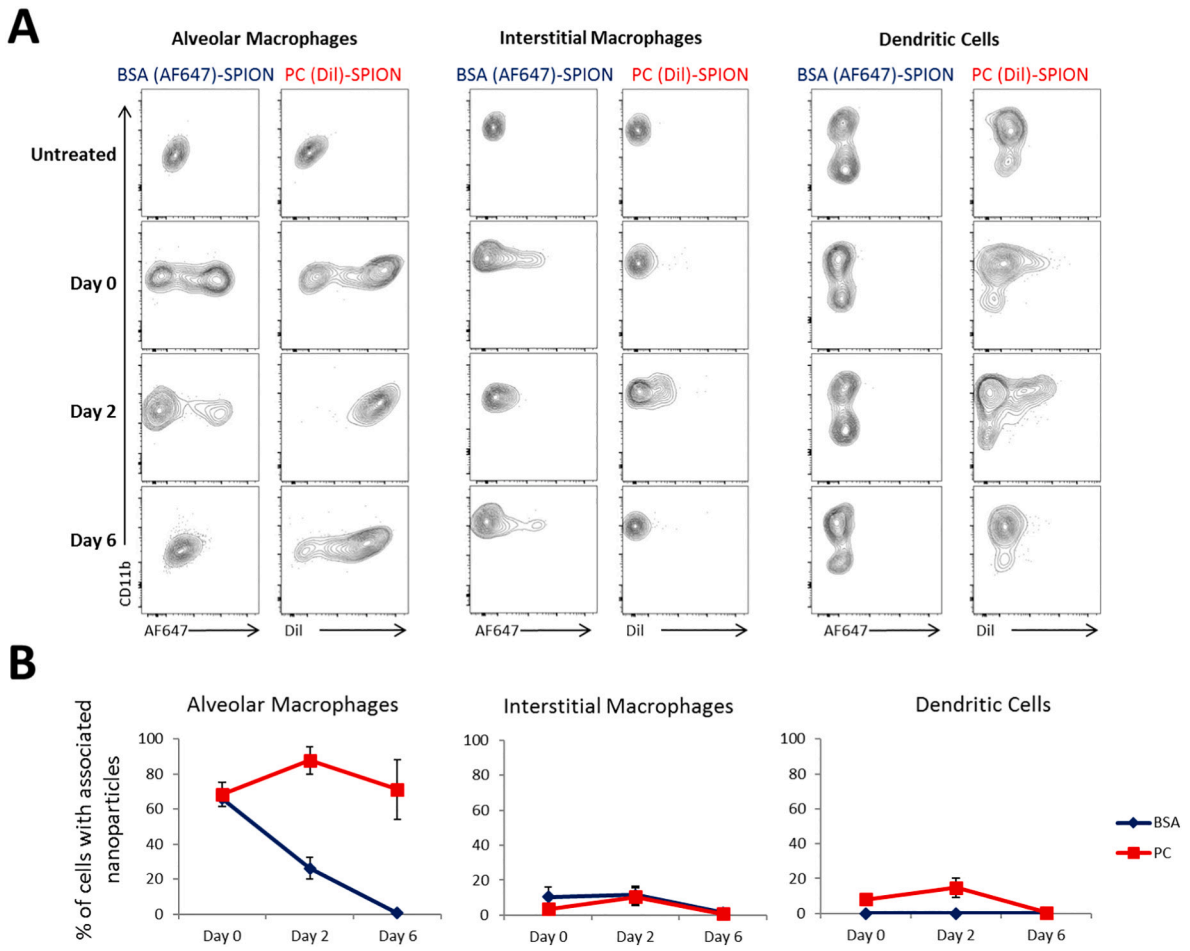

Fig. 5. Cellular distribution of BSA and PC-SPION in the lung. (A) Representative flow cytometric plots showing fluorescence acquisition by myeloid populations in the lung at different times after intratracheal instillation of fluorescent BSA- or PC-SPION. (B) Graphs showing % of cells associated with fluorescent micellar SPION at different times after intratracheal administration. Only fluorescent PC-SPION remained associated with aMϕs 6 days after pulmonary administration. Significantly few resident interstitial macrophages were positive for fluorescent BSA-or PC-SPION. A discrete percentage of inflammatory dendritic cells (MHCII-^{HI}CD11c^{HI}CD103^{neg}CD11b^{HI}F4/80^{neg}) were positive for fluorescent PC-SPION, but not BSA-SPION, at day 0 and 2 after instillation.

3.4. SP-A interaction with PC- and BSA-SPION

To know whether the different retention times of PC- and BSA-SPION may be due to the type of interaction of these NP with components of pulmonary surfactant, we evaluated the possible interaction of SP-A with both PC- and BSA-SPION by quantifying the apparent dissociation coefficient, K_D, and the aggregation state of the SP-A/SPION mixtures. SP-A is traditionally the most abundant protein in the corona formed around NP incubated with human bronchoalveolar lavage fluids [43,44] and SP-A binding to NP is known to affect the nanomaterial colloidal stability and their opsonization prominently [45–47]. The binding of PC-SPION to SP-A was evaluated by following the change in SP-A tryptophan fluorescence. Titration of SP-A with PC-SPION in phosphate-buffered saline decreased the protein's intrinsic fluorescence in a dose-dependent manner (Fig. 6A, left panel), indicating that SP-A binds to PC-SPION. Fitting the titration data at 335 nm to the Hill equation (Fig. 6A, central panel) yielded a K_D value of 45 ± 3 nM and a Hill coefficient, n_H, of 1.16 ± 0.04, indicative of cooperative binding. This K_D value is similar to that obtained for the binding of SP-A to dipalmitoylphosphatidylcholine (DPPC) vesicles ($K_D = 4.3 \pm 0.2$ nM and $n_H = 1.50 \pm 0.04$) (Fig. 6A, right panel). The finding that the n_H values obtained for the binding of SP-A to PC-SPION and DPPC vesicles were greater than 1 correlates with the ability of SP-A to bind multiple ligands in a cooperative manner leading to aggregates [48].

Dynamic light scattering was used to evaluate the effect of SP-A on the size distribution of PC-SPION. In PBS, SP-A (120 nM) exhibited two peaks, at 33 ± 5 nm and 615 ± 3 nm (Fig. 6B), which corresponds to non-aggregated protein particles and NaCl-induced protein aggregates, respectively [35,37]. On the other hand, PC-SPION showed a unique peak, with a mean size of 125 ± 3 nm (Fig. 6B). The addition of SP-A to PC-SPION solutions caused the disappearance of the SP-A peaks and the appearance of a new peak, which presumably consists of SP-A bound at the surface of PC-SPION (Fig. 6B). This new peak exhibited a larger diameter (>2 μm) than that determined for PC-SPION alone, indicating the SP-A-induced agglomeration of PC-SPION. Titration of the nanomaterial with different SP-A concentrations increased the overall average size (*Z*-average) of the SP-A/PC-SPION mixture (Fig. 6C). These results follow the histopathology results, where aggregates of PC-SPION were observed in the alveoli (Fig. S4).

Given that calcium is present in the alveolar fluid at a concentration of 2 mM and that SP-A binds calcium, modifying SP-A conformation and ability to interact with its ligands [32–34,48,49], we studied the effect of physiological calcium concentrations on the colloidal stability of SP-A/PC-SPION mixtures. We used both turbidity and DLS measurements and DPPC vesicles to control phospholipid vesicle aggregation induced by SP-A [33,34,36].

Fig. 7 shows that SP-A (60 nM) addition to either PC-SPION or DPPC suspensions increased sample turbidity. These results correlate with the effect of SP-A on PC-SPION's colloidal stability in the absence of calcium described above. The addition of 2.5 mM calcium slightly increased the

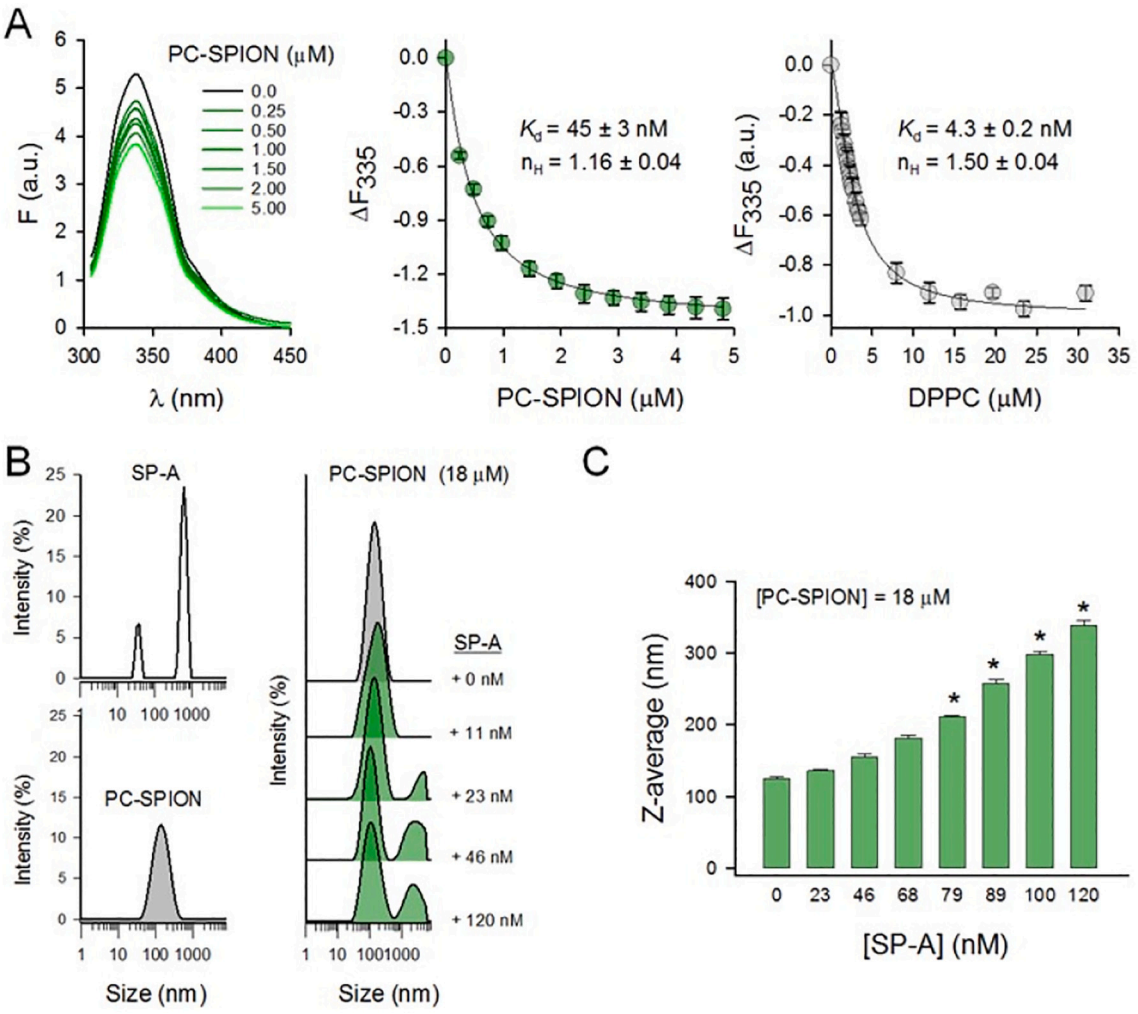

Fig. 6. Binding of PC-SPION to SP-A. (A) Emission fluorescence spectra of SP-A (17.5 nM) (11.4 μg/mL) were recorded on excitation at 295 nm in the absence and presence of increasing concentrations of PC-SPION (0 to 5 μM) (0 to14 μg/mL) at 25 °C in phosphate-buffered saline (PBS) buffer (pH 7.4) (left panel). (B) Effect of SP-A on the intensity-based size distribution of PC-SPION. The left panels show the DLS analysis of the hydrodynamic diameter of PC-SPION and SP-A. The y axis represents the scattered light's relative intensity; the x-axis denotes the particles' hydrodynamic diameter present in the solution. The right panel shows the addition of increasing concentrations of SP-A (0–120 nM) (0–78 μg/mL) to a solution containing a constant concentration of PC-SPION (18 μM). One representative experiment of four is shown. (C) Dependence of Z-average of the different PC-SPION/SP-A mixtures on the concentration of added SP-A. Results are the mean ± SD of four experiments.

amount of scattered light in both samples (Fig. 7). To further characterize the effect of calcium on the aggregation state of mixed SP-A/PC-SPION, samples used for turbidity measurements were analyzed by DLS. Pure SP-A and SPION suspensions were used as controls. The addition of calcium to the SP-A solution promoted the self-association of the protein [36,49], which resulted in the appearance of a single peak centered at 452 ± 3 nm (Fig. 7). For PC-SPION and DPPC vesicles, the addition of Ca^{2+} induced particle clustering in aggregates of different sizes. Calcium further aggregated the SP-A/PC-SPION complex as indicated by the appearance of a new peak with a hydrodynamic diameter larger than those determined for the protein and PC-SPION alone. Likewise, calcium further aggregated SP-A/DPPC mixtures (Fig. 7).

For BSA-coated NP, we determined the binding of SP-A to Alexa Fluor 647-labeled BSA-SPION by following the change in Alexa Fluor 647-labeled NP fluorescence upon addition of increasing amounts of SP-A. Our results show that SP-A bound to BSA-SPION in PBS with high affinity ($K_D = 1.7 \pm 0.2$ fM, $n_H = 1.8 \pm 0.1$) (Fig. 8A). Analysis of the SP-A/BSA-SPION interaction by DLS shows that the addition of SP-A (120 nM) to the BSA-SPION led to the disappearance of the SP-A peaks but did not affect SPION size (125 ± 4 nm) (Fig. 8B). Also, incubation of BSA-SPION with increasing SP-A concentration did not affect nanoparticle *Z*-average (Fig. 8C). The fact that the BSA-SPION hydrodynamic size was not affected by SP-A suggests that SP-A intercalates within the micellar SPION structure rather than adsorbed at the surface. Since SPION cores coated with BSA results in uneven coronas [50], it is likely that SP-A would adsorb to BSA-SPION without displacing BSA molecules from the SPION cores.

Physiological calcium concentrations did not affect the affinity of SP-A for BSA-SPION ($K_D = 0.57 \pm 0.03$ fM, $n_H = 1.8 \pm 0.3$) (Fig. 8D), indicating that calcium is not required for the SP-A/BSA-SPION interaction. Interestingly, calcium slightly increased the size distribution of BSA-SPION in the absence and presence of SP-A, inducing the appearance of two peaks (Fig. 8E). Intriguingly, the first peak was smaller than the BSA-SPION size determined in the absence of this cation (91 ± 2 nm with Ca^{2+} *vs.* 125 ± 4 nm without Ca^{2+}), whereas the second one was larger (295 ± 2 nm). Since BSA self-associates in the presence of calcium (Fig. 8E) and is not strongly bound to the SPION core, it is conceivable that calcium may form ionic bridges between BSA molecules surrounding neighboring NP. As a result, BSA molecules could be detached from some NP, increasing the corona size in other NP. In the presence of calcium, the size distribution of BSA-SPION with further addition of SP-A was similar to its absence (Fig. 8E), and titration of BSA-SPION with

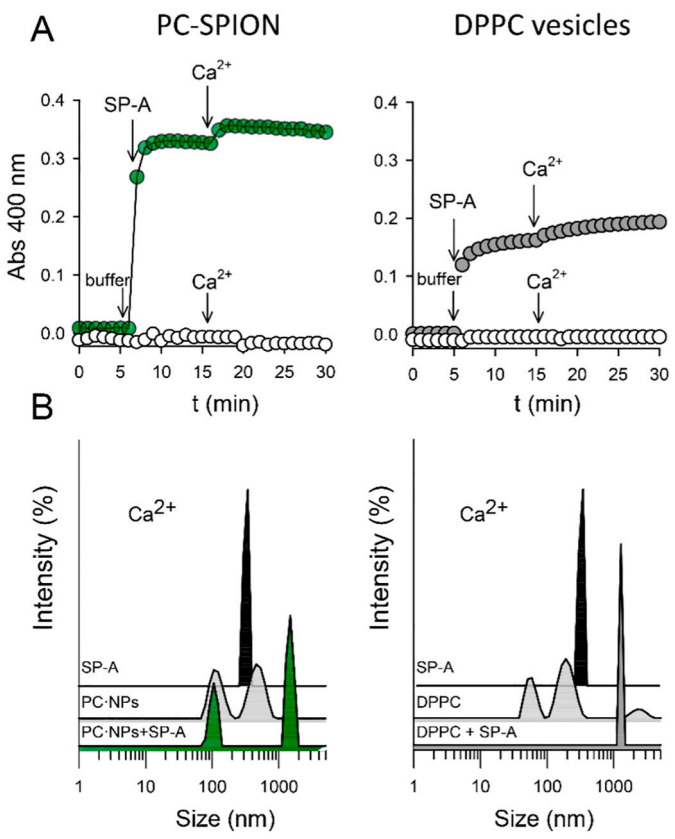

Fig. 7. SP-A aggregates PC-SPION and DPPC vesicles. (A) Sample and reference cuvettes were first filled with either 30 μg/mL of PC-SPION (11 μM) in 5 mM Tris-HCl buffer, pH 7.4, containing 150 mM NaCl. After a 10-min equilibration at 25 °C, SP-A (40 μg/mL) (61 nM) was added to the sample cuvette, and the change in absorbance at 400 nm was monitored. Next, $CaCl_2$ (2.5 mM) was added to both sample and reference cuvettes and the change in absorbance was monitored again. Control experiments were performed adding buffer instead of SP-A to the nanoparticle solution in the reference cuvette. One representative experiment of four is shown. Similar experiments were performed with DPPC vesicles (30 μg/mL) (41 μM). (B) DLS analysis of the effect of 2.5 mM calcium on the size distribution of SP-A, PC-SPION, and DPPC vesicles. In the presence of calcium and NaCl, SP-A aggregates (40 μg/mL) (61 nM) exhibited only one peak centered at 452 ± 3 nm. PC-SPION (18 μM) show two peaks one at 120 nm ± 4, and another at 550 nm ± 3 that corresponded to calcium-induced nanoparticle aggregates. Addition of SP-A to the PC-SPION suspension resulted in the disappearance of the SP-A peak and the shift of the SPION 550 nm-peak to a new peak (>1 μm) with a hydrodynamic diameter larger than those of SP-A and PC-SPION. DPPC vesicles (30 μg/mL) (41 μM) showed a polydispersed size-distribution, with two major peaks centered at 59 ± 2 nm and 190 ± 1 nm, which is independent on calcium. Addition of SP-A caused the disappearance of the DPPC and SP-A peaks and the appearance of a new peak at 1300 ± 4 nm. One representative experiment of four is shown.

increasing amounts of SP-A did not significantly increase the Z-average of these NP (Fig. 8F).

Taken together, our results suggest that the binding of SP-A to micellar BSA-SPION causes negligible NP agglomeration, regardless of the presence or absence of calcium. It is interesting to note that although the binding of SP-A to the BSA-coated nanoparticles does not induce nanoparticle agglomeration, the binding of BSA-SPION to SP-A led to the disappearance of particles corresponding to non-aggregated and self-aggregated SP-A, both in the absence and presence of calcium. Thus, aggregates of SP-A observed in solution disappear as a consequence of BSA-SPION/SP-A interaction. SP-A molecules may intercalate within BSA-SPION, which would prevent the self-aggregation of the protein.

Finally, we assessed the PC- and BSA-SPION aggregation by TEM after exposition to the bronchoalveolar fluid (1 h at 37 °C) isolated from murine lungs, rich in SP-A. Samples were negatively stained to enhance the contrast between the individual micelles. In both samples, we could observe individual micelles with a well-defined coating. However, in the case of PC-SPION, we could observe a higher degree of agglomeration (Fig. S8), which corroborates the PC-SPION/SP-A interaction results obtained with DLS.

3.5. *Effect of PC- or BSA-SPION interaction with SP-A on its immunomodulatory activity*

SP-A is essential to maintain alveolar immune homeostasis [16,17]. It is continuously surveying the extracellular environment for pathogens and quickly activates several mechanisms involved in pathogen phagocytosis by aMϕ [16,17,35]. At the same time, SP-A influences aMϕ responses to limit inflammation, and it is essential for tissue-repair functions of macrophages [16,17,38,51]. The formation of SP-A/PC-SPION aggregates raises the question of whether SP-A sequestered by these aggregated nanoparticles could result in loss of SP-A immunomodulatory functions, leading to uncontrolled inflammation. Therefore, we evaluated the anti-inflammatory activity of SP-A alone and bound to PC- and BSA-SPION (Fig. 9).

Specifically, we evaluated SP-A-induced inhibition of tumor necrosis factor (TNF-α) secretion by rat aMϕs stimulated with bacterial lipopolysaccharide (LPS) and interferon-γ (IFN-γ), as previously reported [38]. As a control, we first verified that the incubation of cells with the two micellar SPION did not induce TNF-α release, which confirms that BSA- and PC-SPION do not generate an inflammatory response in aMϕs. Next, we demonstrated that BSA- or PC-SPION alone did not modify [LPS + IFN-γ]-induced TNF-α release by rat aMϕs and that SP-A bound to either BSA- or PC-SPION maintained its ability to reduce [LPS + IFN-γ]-induced TNF-α secretion to the same extent as SP-A alone. Since SP-A intercalates at the surface of BSA-SPION, it is conceivable that SP-A molecules are available to bind to a great variety of molecules involved in SP-A's immunomodulatory functions. Intriguingly, sequestration of SP-A in PC-SPION aggregates did not affect SP-A's anti-inflammatory activity on stimulated aMϕs. This might be explained by i) the high-order oligomerization of SP-A in umbelliform shaped structures that facilitates multivalent binding to their ligands and ii) the high binding affinity of SP-A to both IFN-γ and the LPS receptor, impeding ligand/receptor interaction and the subsequent activation of macrophages [38].

We also analyzed the binding of SP-A to the surface of a rough Gram-negative bacterium (*E. coli* J5) and subsequent bacterial viability in the presence or absence of surfactant lipids (DPPC vesicles) or the two micellar SPION. SP-A recognizes the lipid A moiety of *Re*-LPS in the outer membrane of *E. coli* J5 by its globular heads [52]. Fig. 10 shows that SP-A bound to BSA-SPION conserved its binding to *E. coli* J5, whereas SP-A bound to PC-SPION or surfactant lipids lost it, indicating that sequestration of SP-A in PC-SPION agglomerates and surfactant lipid vesicles reduces SP-A interaction with *E. coli* J5 bacterial surface. Data supporting the direct antimicrobial activity of SP-A are sparse. Most respiratory pathogenic bacteria and fungi are resistant to SP-A [16,17,35]. However, the cooperative interaction of SP-A with other lung antimicrobial peptides, and antibiotics, could be meaningful in the innate host defense of the lungs [35,53].

Overall, the binding of SP-A with different surfaces leads to different outcomes: nanoparticle aggregation for PC-SPION but not for BSA-SPION. The globular region of SP-A is responsible for interaction of the protein with lung surfactant phospholipids [48] and probably to PC-SPION. The fact that SP-A bound to PC-SPION—but not SP-A bound to BSA SPION—loses its ability to bind to the surface of a rough Gram-negative bacterium (containing Re-LPS) by its globular heads suggests that a domain different than the globular domain is involved in the binding of SP-A to BSA-coated nanoparticles, and therefore not compatible with multivalent aggregation.

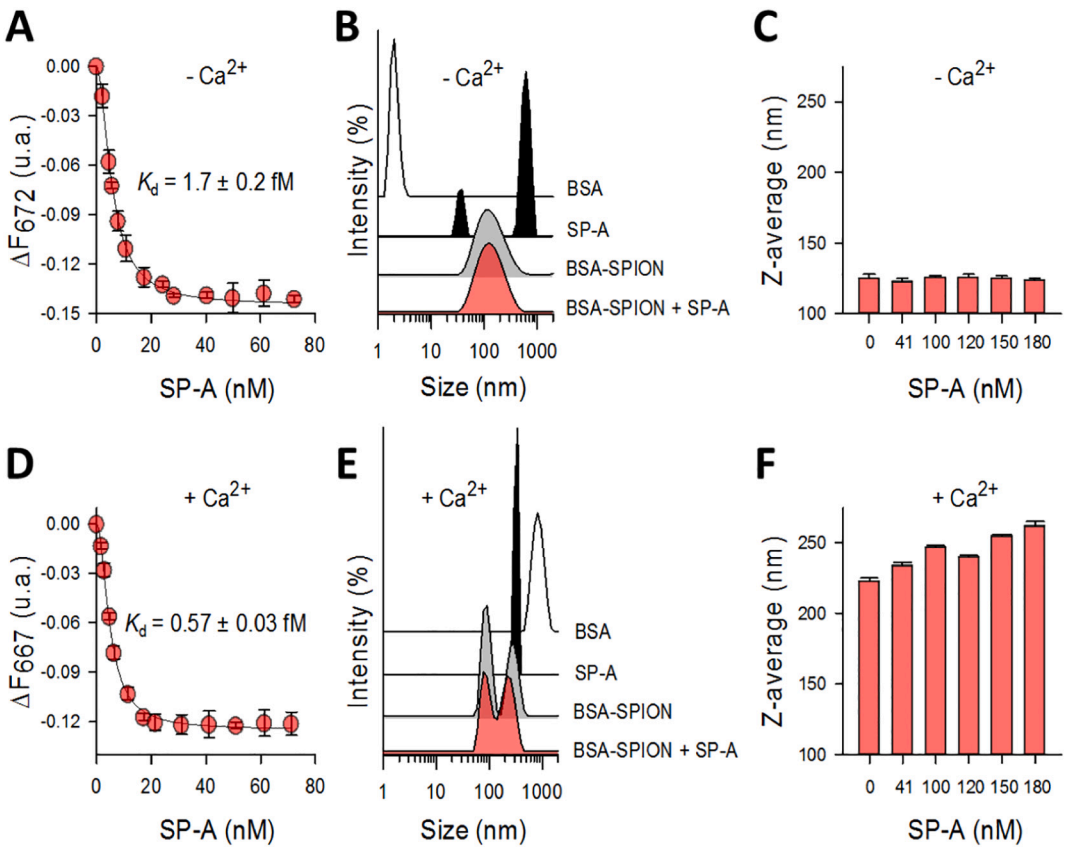

Fig. 8. Binding of SP-A to BSA-SPION. (A) Equilibrium binding titration of BSA-SPION labeled with Alexa Fluor 647 with SP-A. The interaction between SP-A and the SPION was monitored by recording SPION fluorescence as a function of SP-A concentration (0 to 79 nM) (0–51 μg/mL) in PBS buffer. ΔF is the difference in SPION intensity at 672 nm in the presence and absence of protein. The data shown are the mean of four independent measurements. All measurements were performed at 25.0 ± 0.1 °C. (B) DLS analysis of the hydrodynamic diameter of BSA (0.6 μM), SP-A (111 nM) (72 μg/mL), BSA-SPION (96 nM) (50 μg/mL), and the SP-A/BSA-SPION complex in PBS. The y axis represents the scattered light's relative intensity; the x-axis denotes the particles' hydrodynamic diameter present in the solution. One representative experiment of four is shown. (C) Dependence of *Z*-average of different BSA-SPION/SP-A mixtures on the concentration of added SP-A in PBS. Results are the mean ± SD of four experiments. (D) Effect of physiological calcium concentration (2.5 mM) on the equilibrium binding titration of BSA-SPION with SP-A. Measurements were performed as in (A). (E) Intensity-based size distributions of BSA (0.6 μM), SP-A (111 nM) (72 μg/mL), BSA-SPION (96 nM) (50 μg/mL), and the SP-A/BSA-SPION complex in PBS in the presence of 2.5 mM $CaCl_2$. Data represent the mean distribution of four independent measurements. (F) Calcium effect on the overall Z-average of BSA-SPION in the absence and presence of increasing amounts of SP-A. Results are the mean ± SD of four experiments. All measurements were performed at 25.0 ± 0.1 °C.

4. Discussion

The aim of this study was to investigate a theranostic nanoparticle with promising efficiency for local lung-targeted drug delivery. To prepare the micellar SPION, we selected two coatings closely related to biomolecular components present in the alveolar fluid. One is PC, which is the mayor phospholipid class of lung surfactant and is critical in constituting the interfacial film for functional breathing [18]. While this phospholipid has been consistently used in the composition of liposome-based NP to enhance pulmonary drug delivery [1,10,54,55], there are only a few examples of PC being used as a mere coating agent in polymeric or metal oxide-based NP for lung administration [45,46]. The other coating is albumin, which is an endogenous soluble protein prevailing in plasma and in the alveolar fluid, although the estimated albumin concentration in the alveolar fluid is less than 10% of the plasma albumin value [56]. Albumin is already widely used as a natural coating/emulsifier of many nanoformulations to confer enhanced capacity of extracellular retention to the NP [57,58]. PC- and BSA-SPION were similar in size and charge, but we found that they have different residence times in the lung after *in vivo* instillation.

We were able to visualize large amounts of instilled PC-SPION in the alveolus for a long period by non-invasive MRI. The lung is usually challenging to picture by MRI, especially with contrast agents providing a negative signal. Indeed, these contrast agents can be monitored only when their accumulation is evident because of their low sensitivity and darkness of the lung background. We followed the pulmonary retention of PC-SPION for almost one week after instillation by *in vivo* MRI using a specific sequence that provides excellent anatomical details of pulmonary microstructure and is insensitive to the typical signal voids produced by susceptibility artifacts and SPION presence. In contrast, we showed that BSA-SPION was not retained in the lung by *in vivo* MRI experiments. A few hours after BSA-SPION instillation, magnetic resonance images showed evanescence of the contrast originated by the magnetic cores. Progressive appearance of a signal in the liver at days 2 and 6 confirmed the translocation of these NP to the rest of the body.

The different residence times of the BSA- and PC-SPION in the lung were also evaluated by flow cytometry analysis of the association of fluorescent nanoparticles with lung myeloid cells at various times after intratracheal administration. We found that fluorescent PC-SPION remained associated with alveolar macrophages 6 days after pulmonary administration, likely due to the lack of uptake of these nanoparticles by macrophages. Histological analysis showed co-localization of PC-SPION aggregates with macrophages, suggesting that these particles are agglomerated and that they are not easily internalized by alveolar macrophages. Physiologically, alveolar macrophages continuously endocytose small vesicles of inactive lung surfactant, which are

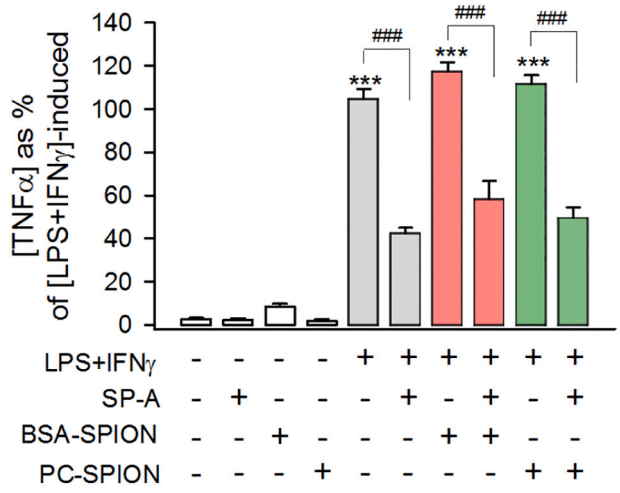

Fig. 9. SP-A bound to BSA- and PC-SPION maintains its immunomodulatory effect. SP-A was pre-incubated with BSA-SPION or PC-SPION for 10 min at room temperature at a weight ratio of 1:1 for (SP-A:BSA-SPION) and 11.4:1 for (SP-A:PC-SPION). Then, SP-A (25 μg/mL), BSA-SPION (25 μg/mL), PC-SPION (2.19 μg/mL), or pre-incubated mixtures of SP-A and BSA- or PC-SPION were added to isolated aMϕs from rat lungs. Cells were stimulated with LPS (1 ng/mL) and IFN-γ (10 ng/mL) for 24 h, and ELISA-measured TNF-α in the extracellular medium is shown. Data are means ± SEM from three different cell cultures and are expressed as % of [LPS + IFN-γ]-induced TNF-α release. The mean value of [LPS + IFN-γ]–induced TNF-α secretion by rat aMϕs in the absence of SP-A was 5.0 ± 0.3 pg/mL (100%). ***$p < 0.001$ compared to untreated cells; $^{###}p < 0.001$ compared between the indicated groups.

formed after compression-expansion cycles. Small vesicles are taken up and degraded by alveolar macrophages as part of the biological life cycle of lung surfactant. However, alveolar macrophages do not internalize large aggregates of surfactant which comprise the surface-active material [18].

In contrast to PC-SPION, fluorescent BSA-coated nanoparticles were cleared promptly after instillation, so that the fluorescent signal associated with alveolar macrophages disappeared on day 2. There are several reasons that might justify the rapid decrease of fluorescent BSA-SPION associated with alveolar macrophages: i) rapid uptake by macrophages and clearance by lysosomal enzymes; ii) rapid passage across the alveolar-capillary barrier and direct entry into the bloodstream; and iii) elimination by the mucociliary escalator system. Several albumin receptors have recently been described. While some of them have been shown to mediate transcytosis across epithelial and endothelial cells, others are more ubiquitously expressed and can bind to conformationally modified albumin, acting as scavenger receptors that deliver modified albumin to lysosomal degradation [59]. Any of these possibilities could sensibly explain the rapid disappearance of BSA-SPION from the lung.

The factors that determine the potential clinical application of NP in the lung depend on the physicochemical properties of NP (size, shape, surface chemical composition) and the interaction of nanoparticles with components of lung surfactant [19,60,61]. The interaction of BSA- and PC-SPION with surfactant components might modify their size, interaction with alveolar cells, and their biological fate. Using electron microscopy, we observed a clear agglomeration of PC-SPION, but no BSA-SPION, after incubation with the bronchoalveolar lavage for 1 h.

Proteomic studies have highlighted those lipids and proteins present in lung surfactant that bind to nanoparticles and form a dynamically changing protein and lipid corona [43,44,60]. Among surfactant proteins, hydrophilic SP-A and SP-D have been found in the corona of different nanomaterials [43,44,60]. SP-A and SP-D are soluble proteins, secreted by the alveolar epithelium and nonciliated bronchiolar cells. They are well-conserved oligomeric proteins, assembled in multiples of three subunits due to their collagen domains. The primary structure of each subunit consists of an N-terminal segment containing cysteine residues involved in oligomerization followed by a collagen-like region, an alpha helical coiled neck region, and a globular domain with a calcium ion at the lectin site. They are intracellularly assembled into oligomeric structures that, in the case of SP-A, resemble a flower bouquet of six trimers, while the assembly of SP-D resembles a cruciform of four trimers [16,17].

Since SP-A is a lipid binding protein and is the most abundant alveolar protein in the corona of nanoparticles (including PC-coated nanoparticles) incubated with the bronchoalveolar lavage or surfactant [43,44,60,61], we investigated whether SP-A can induce PC-SPION aggregation. The interaction of SP-A with the two types of SPION was analyzed in detail by a combination of biochemical and physicochemical techniques. We found that the binding of SP-A to PC-SPION induced particle aggregation, which is consistent with our previous results indicating that SP-A affects the colloidal stability of PC-coated particles [45]. In addition, SP-A-mediated PC-SPION aggregation is in line with SP-A's ability to bind and aggregate phospholipid vesicles [34,36,48]. This SP-A property is important in the lung because the capability of SP-A to bind simultaneously to different bilayers increases the cohesivity

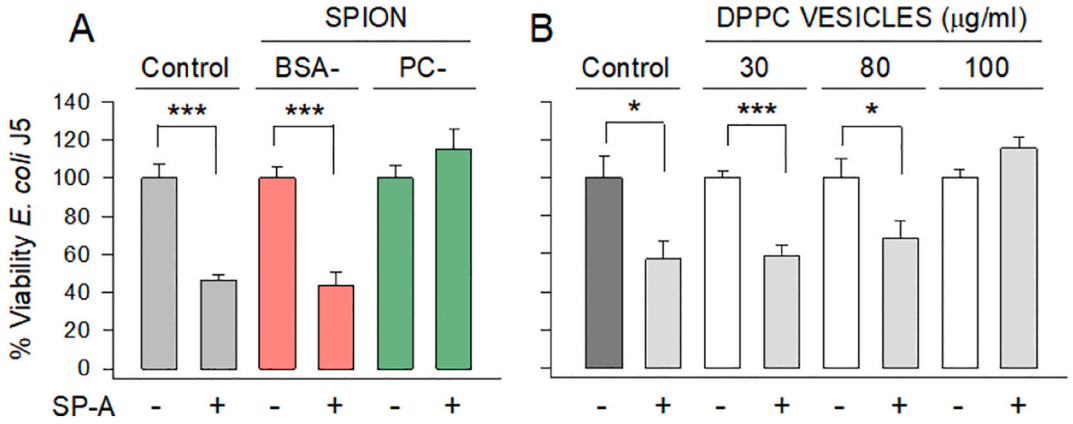

Fig. 10. SP-A bound to PC-SPION or DPPC vesicles loses, while SP-A bound to BSA-SPION retains its binding to the outer membrane of *E. coli* J5. (**A**) SP-A (40 μg/mL) was pre-incubated with BSA-SPION (40 μg/mL) or PC-SPION (3.51 μg/mL) nanoparticles (A) at a weight ratio of 1:1 for (SP-A/BSA-SPION) and 11.4:1 for (SP-A/PC-SPION) for 10 min at room temperature. Then, 300 C.F.U. of *Escherichia coli* J5 were incubated 30 min with each component alone and the pre-incubated mixtures. In (B), SP-A (40 μg/mL) was pre-incubated with DPPC vesicles at the indicated concentrations (30–100 μg/mL) for 10 min, and then 300C.F.U. of *E. coli* J5 were added and incubated with each component alone and the protein-lipid mixtures for 30 min. In A and B, bacterial suspension was plated in agar for colony count. Data are mean ± S.E.M. of colony forming units (C.F.U.) calculated as a % of C.F.U. obtained in the absence of SP-A. *$p < 0.5$, and ***$p < 0.001$ compared to without SP-A.

between surfactant membranes, which helps to sustain low surface tension at the end of exhalation [18].

SP-A also bound to BSA-SPION with high affinity, but binding did not lead to nanoparticle aggregation. SP-A may intercalate among the BSA-coated nanoparticles by a domain not compatible with multivalent aggregation. The globular domains of SP-A are responsible for interaction of the protein with surfactant phospholipids [48], the lipid A moiety of *Re*-LPS [52], and probably PC-coated nanoparticles. Contrary to SP-A bound to PC-SPION, SP-A bound to BSA SPION retained its ability to bind to the surface of a rough Gram-negative bacterium (containing Re-LPS), suggesting that SP-A is bound to BSA-SPION by a domain different than the globular domain.

SP-A behavior towards PC-SPION could be transferable to the *in vivo* context, where, after NP instillation, we have observed agglomeration of PC-SPION in histological lung samples and retention of PC-SPION in the lung. However, we cannot rule out the possible influence of other surfactant proteins and lipids in the agglomeration of PC-coated nanoparticles. Among surfactant proteins, SP-D is found in very small amounts in the corona of PC-coated nanoparticles [60] and does not affect the colloidal stability of PC-coated particles [45]. This is consistent with the fact that SP-D does not bind to DPPC, PC, or other surfactant lipids, except phosphatidylinositol (PI) and glycosphingolipids through a lectin-mediated binding [62]. Given that there is no evidence that SP-A and SP-D interact with each other, we infer that SP-D would not interfere with SP-A-induced nanoparticle agglomeration. On the other hand, hydrophobic SP-C, an α-helical transmembrane protein, does not bind to the nanoparticle surface or interact with SP-A [63]. Thus, it is difficult to conceive that this protein would somehow interfere in the interaction of SP-A with PC-SPION nanoparticles. In contrast, hydrophobic SP-B, a monotopic membrane protein, can interact with SP-A [63]. Thus, it is possible that hydrophobic SP-B would influence the observed agglomeration of PC-SPION nanoparticles together with surfactant lipids. Additional studies will be necessary to further elucidate such interactions on a molecular level.

Toxicological studies indicate that respirable nano-sized particles might cause severe inflammatory reactions [64]. This toxicological effect increases with decreasing particle size and could also be an issue for nanotherapeutic lung delivery [65]. In our study, we did not find evidence of pulmonary inflammation, even in the case of PC-SPION that showed prolonged and considerable accumulation during 7 days after NP administration. Moreover, we showed that neither type of nanoparticle generates an inflammatory response in isolated rat alveolar macrophages.

The direct inflammatory effect in the lungs after administration of NP is not the only parameter inducing toxicity. The potential inactivation of several components of lung surfactant may lead to patient vulnerability. This can be particularly the case for SP-A, which plays a critical role in lung defense and immune response [16,17]. We found that the interaction of both BSA- and PC-SPION with SP-A did not affect SP-A's anti-inflammatory activity on rat alveolar macrophages stimulated with LPS and IFN-γ. Thus, SP-A bound to PC-SPION aggregates can scavenge proinflammatory molecules (such as IFN-γ) as well as SP-A attached to BSA-SPION. However, sequestration of SP-A in PC-SPION aggregates reduced SP-A's interaction with other ligands such as *E. coli* J5 bacterial surface. This may be an issue for delivery to the lung, nonetheless we also observed that sequestration of SP-A in (naturally occurring) PC vesicle aggregates also reduced its binding to *E. coli* J5. It is known that SP-A does not directly combat most respiratory pathogenic bacteria, but instead acts in combination with other antimicrobials to reduce viability of clinically relevant pathogens [35,53]. Therefore, more extensive studies should be done to determine whether PC-SPION nanoparticles impair the bactericidal activity of antimicrobial complexes containing SP-A. In addition, it would be important to explore whether serum proteins such as fibrinogen or C-reactive protein, which increase greatly in the alveolar fluid in respiratory diseases [18,37,39], interfere with the binding of SP-A to nanoparticles and the *in vivo* biological fate of these nanoparticles in inflammatory lung diseases.

5. Conclusions

We have demonstrated how the nature of the coating of two biomedically relevant nanoformulations (PC- and BSA-SPION) can definitively influence their residence time in the lung. Considering that both micellar SPION have similar size and negative charge, one should expect similar behavior of nanoparticles in the alveolar fluid. However, we observed completely different bioavailabilities in the lungs for a period that varied from hours to a few days for BSA-SPION and from days to weeks for PC-SPION. Our results suggest that the longer residence time of instilled PC-SPION in the lung is probably due to a particular behavior of SP-A that induces aggregation of PC-coated nanoparticles, implying a central role of this alveolar protein in the retention time for PC-coated nanoparticles. Due to iron oxide's presence in the core, we could monitor and trace the two nanoformulations' location in the lung by longitudinal MRI experiments in a murine animal model. Overall, several clues indicate that BSA coating might be more suitable for the design of nanoparticles intended for systemic absorption, although more experiments should be performed to unravel the pharmacokinetics of BSA-SPION. On the other hand, PC-SPION nanoparticles remain a long time in the lung without inducing apparent inflammation and can be easily loaded with hydrophobic drugs [66]. Therefore, PC-coating formulations appear promising as theranostic nanopharmaceutic agents for pulmonary drug delivery and could benefit patients by providing high, sustained drug concentrations in the lung tissue with low systemic drug exposure.

Abbreviations

BSA	bovine serum albumin
PC	phosphatidylcholine
SPION	superparamagnetic iron oxide nanoparticles
NP	nanoparticle
PC-SPION	superparamagnetic iron oxide nanoparticles coated with phosphatidylcholine
BSA-SPION	superparamagnetic iron oxide nanoparticles coated with bovine serum albumin
SP-A	surfactant protein A
MRI	magnetic resonance imaging
TEM	electron microscopy
d_h	hydrodynamic diameter
DLS	dynamic light scattering
MEFs	mouse embryonic fibroblasts
UTE	ultrashort echo
aMϕ	alveolar macrophage
K_D	apparent dissociation constant
DPPC	dipalmitoylphosphatidylcholine
TNF-α	tumor necrosis factor
LPS	lipopolysaccharide
IFN-γ	interferon-γ

CRediT authorship contribution statement

Conceptualization: all authors.
Investigation: H.G., S.C-R., O.C., N.A-G., A.V.L-V., B.G-F. and F.H.
Methodology: H.G., S.C-R., O.C., N.A-G., A.V.L-V., and B.G-F.
Writing—original draft preparation: all authors
Visualization: H.G., S.C-R., O.C., B.G-F., C.C., and J.R-C.
Writing—review and editing: H.G., J.R-C., and C.C.
Supervision: C.C. and J.R-C.
Project administration: C.C and J.R-C.
Funding acquisition for this study: C.C. and J.R-C.

All authors read and agreed to the published version of the manuscript.

Declaration of competing interest

The authors declare that they have no known competing financial interests or personal relationships that could have appeared to influence the work reported in this paper.

Acknowledgments

We thank Ligue contre le cancer, comité Charentes Maritimes, which allows us to free up some time to complete this manuscript's redaction during a grant -not fully dedicated on this work- agreed to LIENSs, UMR CNRS 7266, La Rochelle. We thank Julien Cherfan (UMR CNRS LIENSs) for his participation in the cell culture experiments.

Funding sources

This research was funded by the Spanish Ministry of Science and Innovation (Grants SAF2017-84494-C2-R and MAT2015-65184-C2-2-R to J.R-C and SAF2015-65307-R and RTI2018-094355-BI00 to C.C.), Department of Industry, Innovation, Trade and Tourism, Basque Government under the ELKARTEK Program (Grant No. KK-2019/bmG19 to J.R-C). BBVA Foundation (PR[18]_BIO_IMG_0008 to J.R-C) and Ayuda de la Fundación contra la Hipertensión Pulmonar (2018) to J.R-C. This work was also supported by Instituto de Salud Carlos III (CIBERES) to J. R-C and C.C. S.C-R is supported by the grant PID2019-106139RA-100 funded by MCIN. H.G. research is supported by Grants of the Ligue contre le Cancer of Charente-Maritime CD17, Ligue contre le Cancer CSIRGO in particular CD16, CD17, Région Nouvelle Aquitaine (Projet "Nanovect"). CIC biomaGUNE is supported by the Maria de Maeztu Units of Excellence Program from the Spanish State Research Agency – Grant No. MDM-2017-0720.

Appendix A. Supplementary data

Supplementary data to this article can be found online at https://doi.org/10.1016/j.msec.2021.112551.

References

[1] D. Paturi, M. Patel, R. Mitra, A. Mitra, Nasal and pulmonary delivery of macromolecules to treat respiratory and nonrespiratory diseases, in: N. Vij (Ed.), Pulm. Nanomedicine, Pan Stanford Publishing, 2012, pp. 45–102, https://doi.org/10.1201/b12778-4.

[2] A.M. Hillery, A.W. Lloyd, J. Swarbrick (Eds.), Drug Delivery and Targeting for Pharmacists and Pharmaceutical Scientists, Taylor & Francis, London, 2001.

[3] H.L. Kutscher, P. Chao, M. Deshmukh, Y. Singh, P. Hu, L.B. Joseph, D.C. Reimer, S. Stein, D.L. Laskin, P.J. Sinko, Threshold size for optimal passive pulmonary targeting and retention of rigid microparticles in rats, J. Control. Release 143 (2010) 31–37, https://doi.org/10.1016/j.jconrel.2009.12.019.

[4] G. Oberdörster, E. Oberdörster, J. Oberdörster, Nanotoxicology: an emerging discipline evolving from studies of ultrafine particles, Environ. Health Perspect. 113 (2005) 823–839, https://doi.org/10.1289/ehp.7339.

[5] J.C. Sung, B.L. Pulliam, D.A. Edwards, Nanoparticles for drug delivery to the lungs, Trends Biotechnol. 25 (2007) 563–570, https://doi.org/10.1016/j.tibtech.2007.09.005.

[6] M. Howell, C. Wang, A. Mahmoud, G. Hellermann, S.S. Mohapatra, S. Mohapatra, Dual-function theranostic nanoparticles for drug delivery and medical imaging contrast: perspectives and challenges for use in lung diseases, Drug Deliv. Transl. Res. 3 (2013) 352–363, https://doi.org/10.1007/s13346-013-0132-4.

[7] M. Doroudian, R.Mac Loughlin, A. Prina-Mello, Y. Volkov, S.C. Donnelly, A. O' Neill, Nanotechnology in pulmonary medicine, Curr. Opin. Pharmacol. 56 (2021) 85–92, https://doi.org/10.1016/j.coph.2020.11.002.

[8] M.S. Strozyk, S. Carregal-Romero, M. Henriksen-Lacey, M. Brust, L.M. Liz-Marzán, Biocompatible, multiresponsive nanogel composites for codelivery of antiangiogenic and chemotherapeutic agents, Chem. Mater. 29 (2017) 2303–2313, https://doi.org/10.1021/acs.chemmater.6b05471.

[9] A.A. Shvedova, E. Kisin, A.R. Murray, V.J. Johnson, O. Gorelik, S. Arepalli, A. F. Hubbs, R.R. Mercer, P. Keohavong, N. Sussman, J. Jin, J. Yin, S. Stone, B. T. Chen, G. Deye, A. Maynard, V. Castranova, P.A. Baron, V.E. Kagan, Inhalation vs. Aspiration of single-walled carbon nanotubes in C57BL/6 mice: inflammation, fibrosis, oxidative stress, and mutagenesis, Am. J. Physiol.Lung Cell. Mol. Physiol. 295 (2008) L552–L565, https://doi.org/10.1152/ajplung.90287.2008.

[10] M. Smola, T. Vandamme, A. Sokolowski, Nanocarriers as pulmonary drug delivery systems to treat and to diagnose respiratory and non respiratory diseases, Int. J. Nanomedicine 3 (2008) 1–19, https://doi.org/10.2147/IJN.S1045.

[11] M. Lundqvist, J. Stigler, G. Elia, I. Lynch, T. Cedervall, K.A. Dawson, Nanoparticle size and surface properties determine the protein corona with possible implications for biological impacts, Proc. Natl. Acad. Sci. 105 (2008) 14265–14270, https://doi.org/10.1073/pnas.0805135105.

[12] A. Sosnik, J. das Neves, B. Sarmento, Mucoadhesive polymers in the design of nano-drug delivery systems for administration by non-parenteral routes: a review, Prog. Polym. Sci. 39 (2014) 2030–2075, https://doi.org/10.1016/j.progpolymsci.2014.07.010.

[13] S. Carregal-Romero, L. Fadón, E. Berra, J. Ruíz-Cabello, MicroRNA nanotherapeutics for lung targeting. Insights into pulmonary hypertension, Int. J. Mol. Sci. 21 (2020) 3253, https://doi.org/10.3390/ijms21093253.

[14] D.B. Warheit, T.R. Webb, C.M. Sayes, V.L. Colvin, K.L. Reed, Pulmonary instillation studies with nanoscale TiO2 rods and dots in rats: toxicity is not dependent upon particle size and surface area, Toxicol. Sci. 91 (2006) 227–236, https://doi.org/10.1093/toxsci/kfj140.

[15] C.A. Ruge, H. Hillaireau, N. Grabowski, M. Beck-Broichsitter, O. Cañadas, N. Tsapis, C. Casals, J. Nicolas, E. Fattal, Pulmonary surfactant protein A-mediated enrichment of surface-decorated polymeric nanoparticles in alveolar macrophages, Mol. Pharm. 13 (2016) 4168–4178, https://doi.org/10.1021/acs.molpharmaceut.6b00773.

[16] C. Casals, M.A. Campanero-Rhodes, B. García-Fojeda, D. Solís, The role of collectins and galectins in lung innate immune defense, Front. Immunol. 9 (2018) 1998, https://doi.org/10.3389/fimmu.2018.01998.

[17] C. Casals, B. García-Fojeda, C.M. Minutti, Soluble defense collagens: sweeping up immune threats, Mol. Immunol. 112 (2019) 291–304, https://doi.org/10.1016/j.molimm.2019.06.007.

[18] C. Casals, O. Cañadas, Role of lipid ordered/disordered phase coexistence in pulmonary surfactant function 2012 (1818) 2550–2562, https://doi.org/10.1016/j.bbamem.2012.05.024.

[19] R. Guagliardo, J. Pérez-Gil, S. De Smedt, K. Raemdonck, Pulmonary surfactant and drug delivery: focusing on the role of surfactant proteins, J. Control. Release 291 (2018) 116–126, https://doi.org/10.1016/j.jconrel.2018.10.012.

[20] K. Mosbah, J. Ruiz-Cabello, Y. Berthezène, Y. Crémillieux, Aerosols and gaseous contrast agents for magnetic resonance imaging of the lung, Contrast Media Mol. Imaging 3 (2008) 173–190, https://doi.org/10.1002/cmmi.252.

[21] A. Bianchi, F. Lux, O. Tillement, Y. Crémillieux, Contrast enhanced lung MRI in mice using ultra-short echo time radial imaging and intratracheally administrated Gd-DOTA-based nanoparticles: contrast enhanced lung MRI in mice, Magn. Reson. Med. 70 (2013) 1419–1426, https://doi.org/10.1002/mrm.24580.

[22] S. Dufort, A. Bianchi, M. Henry, F. Lux, G. Le Duc, V. Josserand, C. Louis, P. Perriat, Y. Crémillieux, O. Tillement, J.-L. Coll, Nebulized gadolinium-based nanoparticles: a theranostic approach for lung tumor imaging and radiosensitization, Small 11 (2015) 215–221, https://doi.org/10.1002/smll.201401284.

[23] A. Bianchi, D. Moncelet, F. Lux, M. Plissonneau, S. Rizzitelli, E.J. Ribot, N. Tassali, V. Bouchaud, O. Tillement, P. Voisin, Y. Crémillieux, Orotracheal administration of contrast agents: a new protocol for brain tumor targeting: a new protocol to target brain cancer, NMR Biomed. 28 (2015) 738–746, https://doi.org/10.1002/nbm.3295.

[24] A. Woods, A. Patel, D. Spina, Y. Riffo-Vasquez, A. Babin-Morgan, R.T.M. de Rosales, K. Sunassee, S. Clark, H. Collins, K. Bruce, L.A. Dailey, B. Forbes, In vivo biocompatibility, clearance, and biodistribution of albumin vehicles for pulmonary drug delivery, J. Control. Release 210 (2015) 1–9, https://doi.org/10.1016/j.jconrel.2015.05.269.

[25] J. Pellico, A.V. Lechuga-Vieco, E. Almarza, A. Hidalgo, C. Mesa-Nuñez, I. Fernández-Barahona, J.A. Quintana, J. Bueren, J.A. Enríquez, J. Ruiz-Cabello, F. Herranz, In vivo imaging of lung inflammation with neutrophil-specific 68Ga nano-radiotracer, Sci. Rep. 7 (2017) 13242, https://doi.org/10.1038/s41598-017-12829-y.

[26] W.W. Yu, J.C. Falkner, C.T. Yavuz, V.L. Colvin, Synthesis of monodisperse iron oxide nanocrystals by thermal decomposition of iron carboxylate salts, Chem. Commun. (2004) 2306, https://doi.org/10.1039/b409601k.

[27] H. Groult, J. Ruiz-Cabello, J. Pellico, A.V. Lechuga-Vieco, R. Bhavesh, M. Zamai, E. Almarza, I. Martín-Padura, E. Cantelar, M.P. Martínez-Alcázar, F. Herranz, Parallel multifunctionalization of nanoparticles: a one-step modular approach for in vivo imaging, Bioconjug. Chem. 26 (2015) 153–160, https://doi.org/10.1021/bc500536y.

[28] H. Groult, J. Ruiz-Cabello, A.V. Lechuga-Vieco, J. Mateo, M. Benito, I. Bilbao, M. P. Martínez-Alcázar, A. Juan, J. Lopez, F.F.Herranz Vázquez, Phosphatidylcholine-coated iron oxide nanomicelles for in vivo prolonged circulation time with an antibiofouling protein Corona, Chem. Eur. J. 20 (2014) 16662–16671, https://doi.org/10.1002/chem.201404221.

[29] J. Walczak, S. Bocian, T. Kowalkowski, T. Trziska, B. Buszewski, Determination of omega fatty acid profiles in egg yolk by HILIC-LC-MS and GC-MS, Food Anal. Methods 10 (2017) 1264–1272, https://doi.org/10.1007/s12161-016-0655-7.

[30] M.A.N. Hajibagheri, Electron microscopy methods and protocols, humana press, New Jersey (1999), https://doi.org/10.1385/1592592015.

[31] A.V. Lechuga-Vieco, H. Groult, J. Pellico, J. Mateo, J.A. Enríquez, J. Ruiz-Cabello, F. Herranz, Protein corona and phospholipase activity drive selective accumulation of nanomicelles in atherosclerotic plaques, Nanomed. Nanotechnol. Biol. Med. 14 (2018) 643–650, https://doi.org/10.1016/j.nano.2017.12.021.

[32] C. Casals, E. Miguel, J. Perez-Gil, Tryptophan fluorescence study on the interaction of pulmonary surfactant protein a with phospholipid vesicles, Biochem. J. 296 (1993) 585–593, https://doi.org/10.1042/bj2960585.

[33] F. Sánchez-Barbero, G. Rivas, W. Steinhilber, C. Casals, Structural and functional differences among human surfactant proteins SP-A1, SP-A2 and co-expressed SP-A1/SP-A2: role of supratrimeric oligomerization, Biochem. J. 406 (2007) 479–489, https://doi.org/10.1042/BJ20070275.

[34] F. Sánchez-Barbero, J. Strassner, R. García-Cañero, W. Steinhilber, C. Casals, Role of the degree of oligomerization in the structure and function of human surfactant protein A, J. Biol. Chem. 280 (2005) 7659–7670, https://doi.org/10.1074/jbc.M410266200.

[35] J.M. Coya, H.T. Akinbi, A. Sáenz, L. Yang, T.E. Weaver, C. Casals, Natural anti-infective pulmonary proteins. In vivo cooperative action of surfactant protein SP-A and the lung antimicrobial peptide SP-B N, J. Immunol. 195 (2015) 1628–1636, https://doi.org/10.4049/jimmunol.1500778.

[36] M.L. Ruano, E. Miguel, J. Perez-Gil, C. Casals, Comparison of lipid aggregation and self-aggregation activities of pulmonary surfactant-associated protein A, Biochem. J. 313 (Pt 2) (1996) 683–689, https://doi.org/10.1042/bj3130683.

[37] A. Sáenz, A. López-Sánchez, J. Mojica-Lázaro, L. Martínez-Caro, N. Nin, L. A. Bagatolli, C. Casals, Fluidizing effects of C-reactive protein on lung surfactant membranes: protective role of surfactant protein A, FASEB J. 24 (2010) 3662–3673, https://doi.org/10.1096/fj.09-142646.

[38] C.M. Minutti, B. García-Fojeda, A. Sáenz, R. Guillamat-Prats, A. de Lorenzo, A. Serrano-Mollar, Á.L. Corbí, C. Casals, M. de las Casas-Engel, Surfactant protein A prevents IFN-γ/IFN-γ receptor interaction and attenuates classical activation of human alveolar macrophages, J. Immunol. 197 (2016) 590–598, https://doi.org/10.4049/jimmunol.1501032.

[39] C. Casals, J. Arias-Díaz, F. Valiño, A. Sáenz, C. García, J.L. Balibrea, E. Vara, Surfactant strengthens the inhibitory effect of C-reactive protein on human lung macrophage cytokine release, Am. J. Physiol.Lung Cell. Mol. Physiol. 284 (2003) L466–L472, https://doi.org/10.1152/ajplung.00325.2002.

[40] J. Arias-Diaz, I. Garcia-Verdugo, C. Casals, N. Sanchez-Rico, E. Vara, J.L. Balibrea, Effect of surfactant protein a (SP-A) on the production of cytokines by human pulmonary macrophages, Shock 14 (2000) 300–306, https://doi.org/10.1097/00024382-200014030-00010.

[41] M.J. O'Neil (Ed.), The Merck index: an encyclopedia of chemicals, drugs, and biologicals, 15. ed, RSC Publ., Royal Soc. of Chemistry, Cambridge, 2013.

[42] J. Bourquin, A. Milosevic, D. Hauser, R. Lehner, F. Blank, A. Petri-Fink, B. Rothen-Rutishauser, Biodistribution, clearance, and long-term fate of clinically relevant nanomaterials, Adv. Mater. 30 (2018) 1704307, https://doi.org/10.1002/adma.201704307.

[43] A. Kumar, E.M. Bicer, P. Pfeffer, M.P. Monopoli, K.A. Dawson, J. Eriksson, K. Edwards, S. Lynham, M. Arno, A.F. Behndig, A. Blomberg, G. Somers, D. Hassall, L.A. Dailey, B. Forbes, I. Mudway, Differences in the coronal proteome acquired by particles depositing in the lungs of asthmatic versus healthy humans, Nanomed. Nanotechnol. Biol. Med. 13 (2017) 2517–2521, https://doi.org/10.1016/j.nano.2017.06.008.

[44] H. Whitwell, R.-M. Mackay, C. Elgy, C. Morgan, M. Griffiths, H. Clark, P. Skipp, J. Madsen, Nanoparticles in the lung and their protein corona: the few proteins that count, Nanotoxicology 10 (2016) 1385–1394, https://doi.org/10.1080/17435390.2016.1218080.

[45] C.A. Ruge, U.F. Schaefer, J. Herrmann, J. Kirch, O. Cañadas, M. Echaide, J. Pérez-Gil, C. Casals, R. Müller, C.-M. Lehr, The interplay of lung surfactant proteins and lipids assimilates the macrophage clearance of nanoparticles, PLoS ONE. 7 (2012), e40775, https://doi.org/10.1371/journal.pone.0040775.

[46] C.A. Ruge, J. Kirch, O. Cañadas, M. Schneider, J. Perez-Gil, U.F. Schaefer, C. Casals, C.-M. Lehr, Uptake of nanoparticles by alveolar macrophages is triggered by surfactant protein A, Nanomed. Nanotechnol. Biol. Med. 7 (2011) 690–693, https://doi.org/10.1016/j.nano.2011.07.009.

[47] Z. McKenzie, M. Kendall, R.-M. Mackay, H. Whitwell, C. Elgy, P. Ding, S. Mahajan, C. Morgan, M. Griffiths, H. Clark, J. Madsen, Surfactant protein a (SP-A) inhibits agglomeration and macrophage uptake of toxic amine modified nanoparticles, Nanotoxicology 9 (2015) 952–962, https://doi.org/10.3109/17435390.2014.992487.

[48] C. Casals, Role of surfactant protein A (SP-A)/lipid interactions for SP-A functions in the lung, Pediatr. Pathol. Mol. Med. 20 (2001) 249–268, https://doi.org/10.3109/15513810109168821.

[49] M.L. Ruano, I. García-Verdugo, E. Miguel, J. Pérez-Gil, C. Casals, Self-aggregation of surfactant protein A, Biochemistry 39 (2000) 6529–6537, https://doi.org/10.1021/bi000188z.

[50] Q. Peng, S. Zhang, Q. Yang, T. Zhang, X.-Q. Wei, L. Jiang, C.-L. Zhang, Q.-M. Chen, Z.-R. Zhang, Y.-F. Lin, Preformed albumin corona, a protective coating for nanoparticles based drug delivery system, Biomaterials 34 (2013) 8521–8530, https://doi.org/10.1016/j.biomaterials.2013.07.102.

[51] C.M. Minutti, L.H. Jackson-Jones, B. Garcia-Fojeda, J.A. Knipper, T.E. Sutherland, N. Logan, E. Ringqvist, R. Guillamat-Prats, D.A. Ferenbach, A. Artigas, C. Stamme, Z.C. Chroneos, D.M. Zaiss, C. Casals, J.E. Allen, Local amplifiers of IL-4Ralpha-mediated macrophage activation promote repair in lung and liver, Science 356 (2017) 1076–1080, https://doi.org/10.1126/science.aaj2067.

[52] O. Cañadas, I. García-Verdugo, K.M.W. Keough, C. Casals, SP-A permeabilizes lipopolysaccharide membranes by forming protein aggregates that extract lipids from the membrane, Biophys. J. 95 (2008) 3287–3294, https://doi.org/10.1529/biophysj.108.137323.

[53] V. Fraile-Ágreda, O. Cañadas, T.E. Weaver, C. Casals, Synergistic action of antimicrobial lung proteins against Klebsiella pneumoniae, Int. J. Mol. Sci. 22 (2021) 11146, https://doi.org/10.3390/ijms222011146.

[54] O. Cañadas, R. Guerrero, R. García-Cañero, G. Orellana, M. Menéndez, C. Casals, Characterization of liposomal tacrolimus in lung surfactant-like phospholipids and evaluation of its immunosuppressive activity, Biochemistry 43 (2004) 9926–9938, https://doi.org/10.1021/bi036227z.

[55] S. Chono, R. Fukuchi, T. Seki, K. Morimoto, Aerosolized liposomes with dipalmitoylphosphatidylcholine enhance pulmonary insulin delivery, J. Control. Release 137 (2009) 104–109, https://doi.org/10.1016/j.jconrel.2009.03.019.

[56] S.I. Rennard, G. Basset, D. Lecossier, K.M. O'Donnell, P. Pinkston, P.G. Martin, R. G. Crystal, Estimation of volume of epithelial lining fluid recovered by lavage using urea as marker of dilution, J. Appl. Physiol. 60 (1986) 532–538, https://doi.org/10.1152/jappl.1986.60.2.532.

[57] C. Feng, K. Wang, Y. Lin, Z. Song, Y. Lu, J. Liu, D. Zhu, Y. Li, C. Dong, Extracellular retention of a cyclopamine nanoformulation leveraging larger size and more negative charge for improved breast cancer treatment, J. Mater. Chem. B 6 (2018) 1834–1843, https://doi.org/10.1039/C7TB02777J.

[58] E. Miele, G.P. Spinelli, E. Miele, F. Tomao, S. Tomao, Albumin-bound formulation of paclitaxel (Abraxane ABI-007) in the treatment of breast cancer, Int. J. Nanomedicine 4 (2009) 99–105, https://doi.org/10.2147/ijn.s3061.

[59] M. Bern, K.M. Sand, J. Nilsen, I. Sandlie, J.T. Andersen, The role of albumin receptors in regulation of albumin homeostasis: implications for drug delivery, J. Control. Release 211 (2015) 144–162, https://doi.org/10.1016/j.jconrel.2015.06.006.

[60] S.S. Raesch, S. Tenzer, W. Storck, A. Rurainski, D. Selzer, C.A. Ruge, J. Perez-Gil, U. F. Schaefer, C.-M. Lehr, Proteomic and lipidomic analysis of nanoparticle Corona upon contact with lung surfactant reveals differences in protein, but not lipid composition, ACS Nano 9 (2015) 11872–11885, https://doi.org/10.1021/acsnano.5b04215.

[61] Q. Hu, X. Bai, G. Hu, Y.Y. Zuo, Unveiling the molecular structure of pulmonary surfactant Corona on nanoparticles, ACS Nano 11 (2017) 6832–6842, https://doi.org/10.1021/acsnano.7b01873.

[62] Y. Ogasawara, Y. Kuroki, T. Akino, Pulmonary surfactant protein D specifically binds to phosphatidylinositol, J. Biol. Chem. 267 (1992) 21244–21249, https://doi.org/10.1016/S0021-9258(19)36824-3.

[63] M. Martínez-Calle, A. Alonso, J. Perez-Gil, B. Olmeda, Native supramolecular protein complexes in pulmonary surfactant: evidences for SP-A/SP-B interactions, J. Proteome 207 (2019), 103466, https://doi.org/10.1016/j.jprot.2019.103466.

[64] G. Oberdörster, Safety assessment for nanotechnology and nanomedicine: concepts of nanotoxicology, J. Intern. Med. 267 (2010) 89–105, https://doi.org/10.1111/j.1365-2796.2009.02187.x.

[65] N. Prajitha, S.S. Athira, P.V. Mohanan, Bio-interactions and risks of engineered nanoparticles, Environ. Res. 172 (2019) 98–108, https://doi.org/10.1016/j.envres.2019.02.003.

[66] J.R. Upponi, K. Jerajani, D.K. Nagesha, P. Kulkarni, S. Sridhar, C. Ferris, V. P. Torchilin, Polymeric micelles: theranostic co-delivery system for poorly water-soluble drugs and contrast agents, Biomaterials 170 (2018) 26–36, https://doi.org/10.1016/j.biomaterials.2018.03.054.